# Preparation and characteristics evaluation of mono and hybrid nano–enhanced phase change materials (NePCMs) for thermal management of microelectronics.

Adeel Arshad[a,*], Mark Jabbal[a], Yuying Yan[a,b,*]

[a]*Fluids & Thermal Engineering (FLUTE) Research Group, Faculty of Engineering, University of Nottingham, Nottingham NG7 2RD, UK*
[b]*Research Centre for Fluids and Thermal Engineering, University of Nottingham Ningbo China, Ningbo 315100, China*

---

## Abstract

Efficient, clean and quiet thermal management has become a vital challenge in for cooling of electronic devices. To enhance the capability and efficiency of passive thermal management, novel composite materials have been designed by the combination of graphene nanoplatelets (GNPs), multiwall carbon nanotubes (MWCNTs), aluminium oxide ($Al_2O_3$) and copper oxide (CuO) dispersed in the RT–28HC used as a phase change material (PCM). The series of mono and hybrid nano–enhanced phase change materials (NePCMs) were synthesized using constant mass fraction of 1.0 wt.% of each type of nanoparticles to establish the optimum NePCM in terms of thermal properties for efficient thermal management of microelectronics. Various material characteristic techniques such as ESEM, FT–IR, XRD, TGA, DTG, DCS, IRT and thermal conductivity apparatus were used and microstructure, chemical composition, crystallinity, thermal and phase–change heat transfer characteristics were investigated extensively for each sample of NePCM. The results showed good chemical and thermal stability of all NePCMs without changing the chemical structure of RT–28HC. The surface morphology and crystal formation analysis revealed the uniform dispersion of nanoparticles onto the surface of RT–28HC. In comparison of mono and hybrid NePCMs, the results showed the hybrid NePCM at GNPs/MWCTs mass percentage ratio of 75%/25% had the highest thermal conductivity enhancement of 96% compared to the pure PCM having optimum value of phase–change enthalpy of 245.18 J/g. Finally, enhancement in phase transition while melting and thermal properties evidenced that hybrid NePCMs can be used as potential candidate for the thermal management of microelectronics.

---

*Correspondence authors
Email addresses:* `adeel.arshad@nottingham.ac.uk, adeel_kirmani@hotmail.com` (Adeel Arshad), `yuying.yan@nottingham.ac.uk` (Yuying Yan)

**Graphical Abstract**

# 1. Introduction

Dramatic changes in global climate and greenhouse emissions are two major concerns of the world, resulting from the use of fossil fuels. Therefore, there is a need for an energy demand which can fulfil a broad range of renewable and sustainable energy resources such as solar, wind, biomass, geothermal, and wave to overcome the growing demand for fossil fuels. In addition, thermal energy storage (TES) is widely used for various energy conversion and transportation systems in solar energy conversion and thermal management. The three major TES technologies include sensible–heat–storage (SHS), latent–heat–storage (LHS), and thermo–chemical–storage (TCS). LHS has great potential to store the heat due to small variation in temperature and high energy storage density, which is promising for thermal management of electronic devices. Using phase change materials (PCMs) for LHS offers high energy storage density compared with SHS materials. PCMs, especially organic PCMs including paraffins and non–paraffins, exhibit high latent of fusion which make them highly suitable for latent heat storage energy technologies (LHSET). Meanwhile, organic PCMs possess low thermal conductivity which reduces the heat transfer enhancement. To enhance the heat transfer enhancement and TES performance of organic PCMs, some strategies such as encapsulation [1] and shape–stabilization [2] have been carried out. There are several thermal conductive materials (TCMs) which have been embedded with PCMs to overcome their low thermal conductivity such as metal–fins [3, 4, 5, 6, 7, 8, 9], metal–foam [10], carbon additives [11, 12, 13, 14], metallic and metal oxides nanoparticles [13, 15, 16, 17, 14].
Various carbon–based additives, including carbon nanotubes (CNTs) [18, 19, 20, 21, 22], carbon nanofiber (CF) [23, 24, 25], graphene (GE) [18, 20], graphene oxide (GO) [17, 26], graphite [17, 18, 20], expanded graphite (EG) [27], graphene nanoplatelets (GNPs) [17, 22, 25] and graphite nanoplatelets [25, 28] have been used as TCMs, to prepare and characterize the nano–enhanced phase change materials (NePCMs) for thermal management and TES. The thermal conductivity of NePCMs depends not merely on the innate thermal conductivity of the nanoparticles but it also strongly depends on the interactional compatibility of the PCM and nanoparticles. In earlier studies, Choi et al. [18] used MWCNTs, graphite and graphene as TCMs and determined the thermal conductivity of the NePCM for TES applications. The authors used the poly vinyl pyrrolidone (PVP) as a surfactant and stearic acid as a PCM. The maximum thermal conductivity was found to be 21.5% using graphene of 0.1 vol.% with PVP. Pristine CNTs and grafted CNTs with paraffin–based NePCM was prepared by Li et al. [19]. The results showed that grafted CNTs were shorter in size than

pristine CNTs and the better dispersibility with PCM was found with grafted CNTs. In addition, grafted CNTs had the higher thermal conductivity than pristine CNTs/paraffin NePCMs. Li et al. [20] used MWCNTs graphene and graphite mixed into stearic acid with two mass percentages of 1.0% and 5.0%. The heat transfer performance and thermal conductivity analysis were carried out and the results revealed that the thermal conductivity of graphite–based NePCMs at 5.0% mass percentage was 12 times higher than the pure stearic acid. Bahiraei et al. [25] synthesized three types of carbon-based nanoparticles namely carbon nanofibers, graphene nanoplatelets and graphite nanoplatelets with paraffin wax as a PCM. The results showed the graphite–based NePCM with 7.5% and 10% mass fractions had the best thermal performance for thermal management applications. Warzoha and Fleischer [28] examined single and multilayer graphene into paraffin PCMs from graphene layers from 3 to 44. It was observed that thermal conductivity enhancement of graphene-mixed paraffin PCMs was due to the presence of graphene nanoparticles, which was a stronger function of bending stiffness of graphene than its intrinsic thermal conductivity. Recently, Zou et al. [22] prepared and studied the thermal conductivity and charging/discharging behaviour of MWCNTs, graphene and MWCNTs/graphene based NePCMs using paraffin wax as PCM. The results showed that hybrid MWCNTs/graphene based NePCMs had the higher thermal conductivity.

Similarly, several researchers have used various types of metallic and metal oxides nanoparticles such as Ag [29], Cu [30], $Al_2O_3$ [29, 30, 30, 31, 32, 33, 34, 35, 36], CuO [29, 37, 38], MgO, $TiO_2$ [30, 39, 40], $SiO_2$ [30, 34, 35, 36], $Fe_2O_3$ [34, 36], and ZnO [34, 36]. Bashar and Siddiqui [29] used four different types of nanoparticles, Ag, CuO, $Al_2O_3$ and MWCNTs and mixed with paraffin wax. It was found that the heat transfer coefficient was 18% and 14% higher with CuO and Ag, respectively, than the pure paraffin wax. Nourani et al. [31, 32] synthesised paraffin wax and $Al_2O_3$ based NePCMs with 0.5, 5, 7.5, and 10 wt.% of $Al_2O_3$ and used sodium stearoyl lactylate (SSL) as a surfactant to improve the dispersion stability of $Al_2O_3$ nanoparticles. Results showed effective thermal conductivity enhancement ratios of 31% and 13% at 10.0 wt.% in solid and liquid states, respectively. Colla et al. [33] prepared NePCM using $Al_2O_3$ and carbon black (CB) of 1.0 wt.% with RT20 and RT25 as PCMs. Thermal conductivity of 0.234 and 0.242 W/m.K was achieved with RT20/$Al_2O_3$ and RT25/$Al_2O_3$, respectively, and for RT20/CB and RT25/CB it was 0.344 and 0.323 W/m.K, respectively. Li et al. [30] used calcium chloride hexahydrate ($CaCl_2 6H_2O$) as a PCM with $\gamma-Al_2O_3$ and studied the phase change behaviour, super cooling, thermal conductivity and latent heat of

NePCMs. A maximum thermal conductivity of 1.373 W/m.K was achieved at 2.0 wt.% of $\gamma-Al_2O_3$. Babapoor and his co–authors [34, 36] measured the thermal properties and heat storage characteristics of $SiO_2$, $Al_2O_3$, $Fe_2O_3$, ZnO and hybrid of all nanoparticles mixed into paraffin wax in solid and liquid states. The highest enhancement was obtained with $Fe_2O_3$ at 8 wt.%, however, the authors proposed that $Al_2O_3$ was most suitable for thermal management application. Chieruzzi et al. [35] synthesised NePCMs using $SiO_2$, $Al_2O_3$ and a hybrid of $SiO_2/Al_2O_3$ of 1.0 wt.% and potassium nitrate ($KNO_3$) as PCM. The results found that $SiO_2$ nanoparticles had the best results of decreasing onset temperatures by $2-3°C$ and increasing specific heat by 9.5%. Pahamli et al. [37] dispersed 2 wt.% and 4 wt.% of CuO into PCM, paraffin RT50 and found a maximum thermal conductivity enhancement of 3.9% and 7.2%, respectively, during the phase change state. Praveen and Suresh [38] studied the thermal, chemical and heat transfer performance of solid–solid neopentyl glycol (NPG) and CuO NePCMs for thermal management application. A maximum thermal conductivity of 0.61 W/m.K was obtained at 3.0 wt.% of CuO. The lowest value of phase change enthalpy obtained was 112.4 kJ/kg at 3.0 wt.% of CuO. Sharma et al. [39] prepared a NePCM using $TiO_2$ with mass fractions of 0.5, 1.0, 3.0, and 5.0% and palmitic acid. A maximum thermal conductivity of 0.35 W/m.K and minimum latent heat of 180.03 kJ/kg was obtained at 5.0 wt.% of $TiO_2$. Zhichao et al. [40] used erythritol as PCM and $TiO_2$ of 0.1 vol.%, 0.2 vol.%, 0.5 vol.%, 1.0 vol.% and 2.0 vol.% volume fractions. It was found that the heat capacity of NePCMs was significantly enhanced by 45% and 14% in solid and liquid states, respectively, compared to pure erythritol at 0.2 vol.% of $TiO_2$. Recently, Putra et al. [41] prepared the shape-stable PCMs using the Beewax as a PCM and MWCNTs as TCM with ratios of 5 and 20 wt.%. The authors found the thermal conductivities of 0.46 and 0.58 W/m.K with weight ratios of 5 and 20 wt.%, respectively of MWCNTs. Further, they found the melting temperatures of 60.2°Cand 59.8°C, and latent heat values of 115.5 and 91.6 J/g with 5 and 20 wt.% weight ratios of MWCNTs, respectively. He et al. [42] synthesised the NePCMs using myristic acid as a PCM and dispersed the GNPs, MWCNTs and nano– graphite with weight concentrations of 1, 2 and 3 wt.%. The authors found the best thermal performance with GNPs followed by MWCNTs and nano–graphite. The enhancement in thermal conductivity was achieved by 76.26%, 47.30% and 44.01% for GNPs, MWCNTs and nano–graphite, respectively, under the weight concentration of 3 wt.%. Zhang et al. [43] prepared the NePCMs using n–eicosane as PCM, $SiO_2$ as supporting matrix and EG as TCM with weight concentrations of 3, 5 and 7 wt.%. It was found that melting and

6

solidifying latent heats were 135.80 J/g and 125.93 J/g, respectively, at 7 wt.% of EG and thermal conductivity enhancement was enhanced by 2.37 times in $SiO_2$/n–eicosane NePCM without EG.

In order to increase the thermal enhancement of PCMs, the present study aims to improve the thermal conductivity of PCM and to maintain its heat storage capacity at an optimum level. Mono and hybrid nano–enhanced phase change materials (NePCMs) were synthesized by dispersing carbon–based (GNPs and MWCNTs) and metal oxides–based (CuO and $Al_2O_3$) nanoparticles at constant mass fraction of 1.0 wt.%. Further, morphology, chemical and thermal properties are characterized using various characterization techniques.

## 2. Experimental procedure

### 2.1. Materials

Commercial grade of paraffin, namely RT–28HC, is used as a PCM with melting temperature of $27-29°C$ in the current study. The thermophysical properties of PCM are listed in Table 1. Graphene nanoplatelets (GNPs) of lateral diameter $< 10$ $\mu$m and $98 \pm 1.0\%$ purity of carbon were purchased from 2–Dtech Ltd/Versarien PLC, UK [44]. Multiwall carbon nanotubes (MWCNTs) of outer diameter $5-15$ nm and length of $10-30$ $\mu$m, and purity $> 95$ wt.% were purchased from Carbon Nanotubes Plus, USA [45]. Nanoparticles of copper oxide (CuO) of $< 50$ nm, aluminium oxide ($Al_2O_3$) of 13 nm, and Sodium dodecylbenzene sulfonate (SDBS), were purchased from Sigma–Aldrich, UK [46]. All materials were used without performing any further chemical processing.

Table 1: *Thermal properties of RT–28HC.*

| Melting temperature (°C) | Thermal conductivity (W/m.K) | Latent heat (J/kg.K) | Specific heat (J/kg.K) | Density (kg/m³) |
|---|---|---|---|---|
| 27–29 | 0.2 | 250,000 | 2000 | 880 (solid) 770 (liquid) |

### 2.2. Preparation of NePCMs

A well–precise, two–step method was adopted to synthesize the mono and hybrid–NePCM by using PCM (RT–28HC) and nanoparticles (GNPs, MWCNTs, CuO and $Al_2O_3$). RT–28HC was used as base PCM and a constant mass fraction of $1.0 wt.\%$ of GNPs, MWCMTs, CuO, $Al_2O_3$ GNPs/MWCNT and CuO/$Al_2O_3$ was dispersed as a thermal conductivity enhancer (TCE) medium. Firstly, RT–28HC was melted by heating it at constant

temperature of 50°C in a hot–water bath. After complete melting of RT–28HC, SDBS in the ratio of 4 : 1% of nanoparticles was added as a surfactant (capping agent) for uniform dispersions of nanoparticles into the RT–28HC. The solution of RT–28HC and SDBS was mixed homogenously at a stirring rate of 450 rpm for 30 mins. Thenceforth, constant amount of GNPs, MWCMTs, CuO, $Al_2O_3$ GNPs/MWCNT and CuO/$Al_2O_3$ were added at a constant mass of 1.0 wt.% separately to prepare the six different samples of the mono and hybrid–NePCM. Further, the mixtures were stirred at a stirring rate of 450 rpm for 2.5 hrs for stable and uniform dispersions of nanoparticles. While adding the GNPs, MWCNTs, CuO and $Al_2O_3$ simultaneously, the total mass percentage was 1.0 wt.% and the mass ratio of GNPs/MWCNTs and CuO/$Al_2O_3$ was 75%/25%. Secondly, to minimize agglomeration and sedimentation and to improve more homogeneous and stable dispersion of nanoparticles, ultrasonication was performed on the mixture for 60 mins while maintaining a constant temperature of 50°C using an ultrasonic vibrator at a frequency of 40 kHz [39, 47].
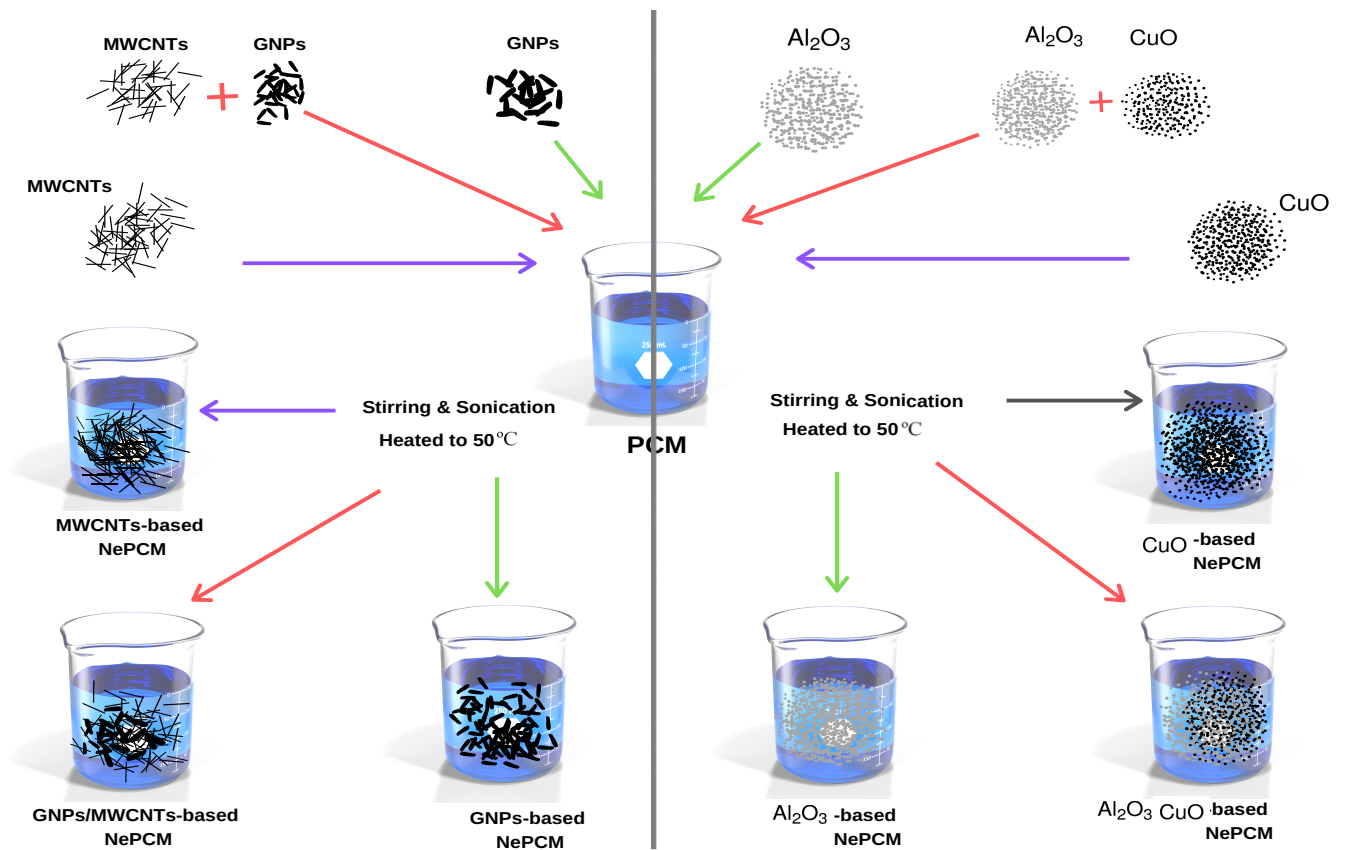


Figure 1: *Preparation process of NePCMs with GNPs, MWCNTs, CuO and $Al_2O_3$.*

## 2.3. Characterizations methods

The morphology, chemical and thermal properties of NePCM were characterized using various facilities as described herein.

### 2.3.1. Environmental Scanning electron microscopy (ESEM) and Energy–dispersive X–ray spectroscopy (EDX)

The surface morphology, microstructure and uniform dispersion of NePCM was examined using an environmental scanning electron microscopy (ESEM, FEI Quanta–650). To determine the elemental composition and surface elemental distribution of NePCM, energy–dispersive X-ray spectroscopy (EDX) analysis was used.

### 2.3.2. Fourier–transform infrared spectroscopy (FTIR)

The chemical composition and functional groups were determined using Fourier–Transform Infrared Spectroscope (FTIR, Bruker Tensor–27 FT–IR Spectrometer) between the wave range of $400 - 4000$ cm$^{-1}$, with a spectral resolution of 4 cm$^{-1}$ and wavenumber accuracy of 0.01 cm$^{-1}$.

### 2.3.3. X–ray diffraction (XRD)

X–ray diffraction (XRD) pattern was measured by an X–ray diffractometer (XRD, Bruker D8 Advance with Da Vinci [48]) between the angle range of $5°$ to $60°$ to visualize the crystalloid phase and crystallographic structure of NePCM. The x–ray tube generates copper k–alpha x–rays, which is often abbreviated to Cu–K$\alpha$ ($\lambda = 1.5406 \mathring{A}$). The x–ray tube runs at 40 kV and 40 mA.

### 2.3.4. Thermogravimetric analysis (TGA) and derivative thermogravimetry (DTG)

The weight loss and thermal stability of NePCM were predicted using thermogravimetrical analysis (TGA) and rate of decomposition of NePCM was predicted using derivative thermogravimetry (DTG) curves simultaneously using TGA/DSC (SDT–Q600 TA instrument Inc., UK) with a balance precision of 0.1 $\mu$g (Error $\pm 0.1$ $\mu$g) [49]. The samples ($4 - 7$ mg) were placed in an aluminium pan and heated from 20°C to 400°C at a rate of 10°C/min under a purified nitrogen atmosphere flow rate of 100 mL/min.

### 2.3.5. Differential scanning calorimeter (DSC)

The phase change properties such as phase change melting/solidification temperatures and latent heat of fusion were measured for pure PCM and NePCMs using a TA instrument differential scanning calorimeter (DSC–2500, TA instrument Inc., UK) equipped with the cooling attachment, under a purified nitrogen atmosphere [50]. The accuracy of the calorimeter was within $\pm 0.04\%$ and temperature precision was $\pm 0.005$°C. All measurements

of DSC were taken at constant heating/cooling of 1 °C/min between 10°C and 50°C. A precise amount of sample mass in the range of $3 - 5$ mg was placed inside a T–zero Hermetic aluminium pan at room temperature and sealed with a lid to ensure full contact between the sample and pan.

### 2.3.6. Thermal conductivity measurement

To measure the thermal conductivity of pure PCM and NePCMs, TCi$^{TM}$ Thermal Conductivity Analyser (C–THERM Technologies Ltd. Canada) was used at a constant temperature of 25°C, which is based on a modified transient plane source (MTPS) method and confirms the ASTM D7984 [51]. The instrument measures thermal conductivity within the range from 0 to 500 W/mK with an accuracy and precision of 5% and 1%, respectively. The sample of 20 mm diameter and thickness from $3 - 5$ mm was prepared. At a specific temperature, fifteen readings were recorded for each NePCM and the average value taken. Three measurements were recorded for each sample at constant temperature and averaged value was reported. A maximum relative error of $\pm 2.0\%$ was found. The uncertainty of measurement was estimated within $\pm 1.0\%$.

### 2.3.7. Infrared thermography (IRT) test

Infrared thermography (IRT) tests were performed to evaluate the temperature-regulating property of pure RT–28HC, mono and hybrid NePCM by using an IR thermographic camera (FLIR–SC2600–EA2). Each sample was filled in a beaker and then immersed in a pot of water on a hot–plate at constant temperature.

## 3. Results and discussions

### 3.1. Morphological and elemental analysis

The surface morphological characteristics and microstructures of prepared mono and hybrid NePCMs based on GNPs, MWCNTs, CuO and Al$_2$O$_3$ were examined by ESEM. Figure 2 presents the surface microstructural features of pure RT–28HC, RT–28HC/GNPs, RT–28HC/MWCNTs, and RT–28HC/GNPs+MWCNTs. The uniform dispersion of GNPs and MWCNTs can been seen in the RT–28HC from the ESEM images, as shown in Figures 2b–2d. The uniform distribution of carbon-based additives within the PCM is because of the repulsive bonding of the SDBS which was used as a dispersant. The mass fraction of GNPs and MWCNTs was very low (1.0 wt.%), however, these are well dispersed and

embedded enough to show their presence. In addition, the presence of these highly thermally conductive carbon–based additives plays a significant role in enhancement of thermal conductivity and thus enhance the heat transfer ability of RT–28HC. Figure 2d shows the morphological structure of hybrid NePCM, RT–28HC/GNPs+MWCNTs which shows effective three-dimensional paths of carbon–based additives. These three-dimensional paths of hybrid NePCM would be an effective mode to transfer the heat in all regions of the RT–28HC. Thus, two different mass percentage of GNPs and MWCNTs having different morphology may obtained good harmonious effects of heat transfer enhancement.

The microstructure of CuO and $Al_2O_3$ based metallic oxide nanoparticles in hybrid NePCM, RT–28HC/CuO+$Al_2O_3$ of 1.0 wt.%, is presented in Figure 3. Figure 3a shows the ESEM image using low vacuum secondary electron (LFD) detector, whereas Figure 3b shows the ESEM image using backscatter electron (BSE) detector for low vacuum mode. From Figure 3a and 3b, it can be observed by the zones with the presence of non–homogenous aggregates of CuO+$Al_2O_3$ nanoparticles on the surface of pure RT–28HC. Similar observations have been reported by Chieruzzi et al. [34] with $SiO_2$/$Al_2O_3$ of 1.0 wt.%. Although the mass fraction of both nanoparticles (CuO+$Al_2O_3$) is very low, 1.0 wt.%, the percentage of CuO is 75% of 1.0 wt.% which may cause the small patches of aggregates due to its higher density compared to the $Al_2O_3$ and RT–28HC. For better visualization and understanding, energy–dispersive X–ray spectroscopy (EDX) maps and elemental composition of RT–28HC/CuO+$Al_2O_3$ are shown in Figures 4 and 5, respectively. Figure 4a–4d shows the distribution of carbon (C), aluminium (Al), oxygen (O) and copper (Cu), respectively; elements present in the hybrid NePCM of RT–28HC/CuO+$Al_2O_3$. In Figure 4a, the red colour shows the presence of C element in different regions of the material of RT–28HC PCM, while the dark colour represents the aggregates of Cu, Al and O elements. Similarly, green, purple, and brown colours represent the aggregates of Al, O and Cu elements present in compounds of CuO, $Al_2O_3$ and RT–28HC. The presence of all elements C, Al, Cu and O in different colours can be seen in Figure 4e. A clear observation of aggregates of nanoparticles can be seen in different regions of the NePCM. The elemental composition of all four elements present in CuO, $Al_2O_3$ and RT–28HC can been identified from Figure 5. It is revealed from Figure 5 that the weight percentage of all elements in hybrid NePCM consisting of CuO, $Al_2O_3$ and RT–28HC is equal according to their compositions used in the mixture. From the elemental mapping and composition analysis, it can been seen that CuO nanoparticles are more dispersed than the $Al_2O_3$ within RT–28HC, as per the used
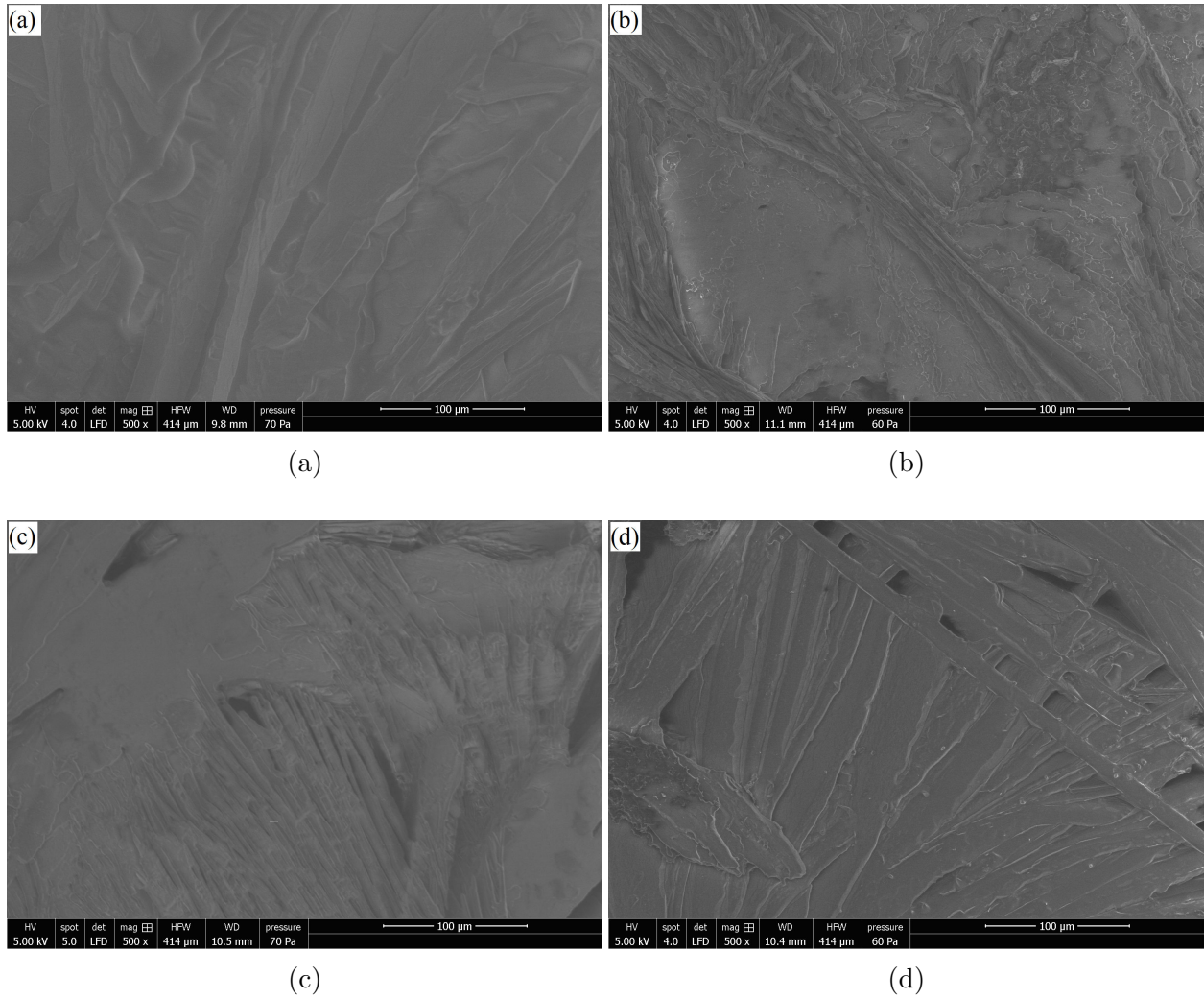
Figure 2: *ESEM images of (a) RT–28HC, (b) RT–28HC/GNPs, (c) RT–28HC/MWCNTs, and (d) RT–28HC/GNPs+MWCNTs.*
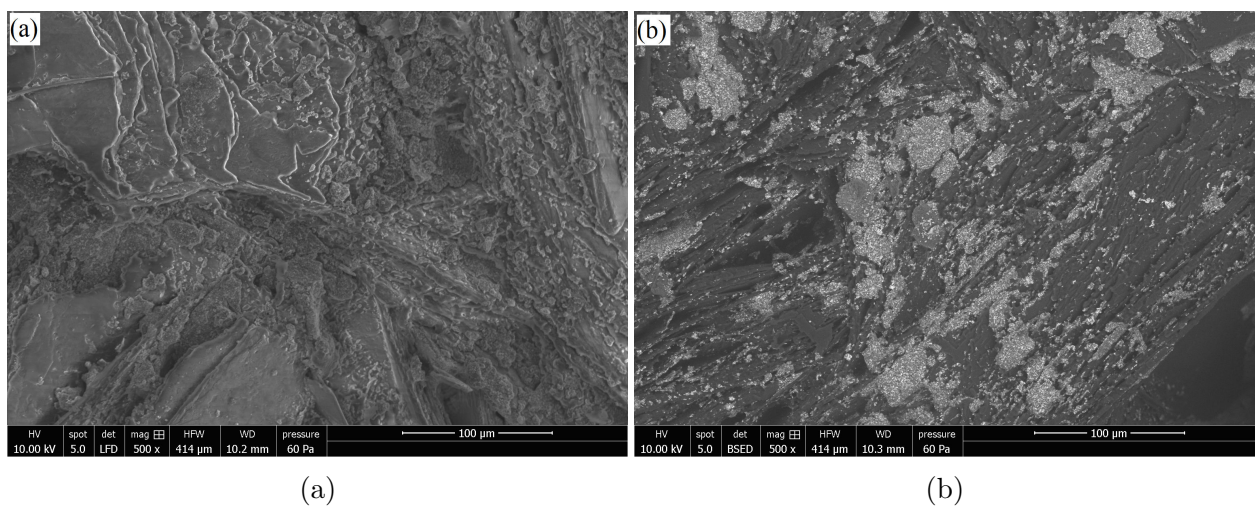


Figure 3: *ESEM images of RT–28HC/$Al_2O_3$+CuO (a) LFD and (b) BSED.*

percentage of CuO/Al$_2$O$_3$. In addition, ESEM and EDX show agglomeration of nanoparticles. Similar observations have been reported by Chieruzzi et al. [35]. Therefore, better and more uniform dispersion of the nanoparticles can be achieved by using smaller sized nanoparticles [52, 53].

*3.2. FT–IR analysis*

The chemical interaction of carbon–based (GNPs and MWCNTs) and metallic oxide–based (CuO and Al$_2$O$_3$) nanoparticles in mono and hybrid NePCMs were characterized by FT–IR spectroscopy. Figure 6 shows the transmittance band of FT–IR spectra of GNPs, MWCNTs, RT–28HC, RT–28HC/GNPs, RT–28HC/MWCNTs and RT–28HC/GNPs+MWCNTs between wave numbers of 500 and 3500 cm$^{-1}$. There are not significant stretching and bending peaks observed of infrared spectra of MWCNTs and GNPs because of the absence of functional groups. For the spectrum of RT–28HC, three transmittance peaks at 2955 cm$^{-1}$, 2913 cm$^{-1}$, 2847 cm$^{-1}$ represent the medium symmetrical stretching vibration of C–H alkane group. The peak at 1470 cm$^{-1}$ identifies the medium C–H scissoring of –CH$_2$– and –CH$_3$ group in RT–28HC. The peak at 718 cm$^{-1}$ represents the weak rocking vibration of C–H in long-chain methyl group. The bands observed at 633 cm$^{-1}$ and 541 cm$^{-1}$ correspond to the deformation vibration of C–H. The FT–IR spectrum of RT–28HC/GNPs, RT–28HC/MWCNTs and RT–28HC/GNPs+MWCNTs shows neither any significant new peak nor any major peak shifts in the NePCMs, which indicates that there is an only physical interaction of RT–28HC, GNPs, MWCNTs and SDBS. Therefore, infrared spectrum results indicate that there is no rearrangement of the functional group, which reveals that no chemical reaction takes place between RT–28HC, GNPs and MWCNTs. Figure 7 presents the FT–IR spectrum results of CuO, Al$_2$O$_3$, RT–28HC, RT–28HC/Al$_2$O$_3$, RT–28HC/CuO and RT–28HC/Al$_2$O$_3$+CuO. In the case of CuO nanoparticles, there are two stretching bands at 880 cm$^{-1}$ and 1432 cm$^{-1}$ which represent the characteristics bands of Cu–OH functional group [54, 55]. Moreover, a small peak can be observed at 729 cm$^{-1}$ which indicates the standard adsorption spectra pattern of the amorphous structure or disordered defects of $\gamma-$Al$_2$O$_3$ [56]. The FT–IR spectrums of RT–28HC/Al$_2$O$_3$, RT–28HC/CuO and RT–28HC/Al$_2$O$_3$+CuO exhibit similar trends as GNPs and MWCNTs based mono and hybrid NePCMs, as shown in Figure 6. It can be seen that Al$_2$O$_3$ and CuO based mono and hybrid NePCMs do not exhibit any major new peak or peak shifts which represent only the physical interaction of Al$_2$O$_3$ and CuO nanoparticles in NePCMs. Similar trends of infrared

13
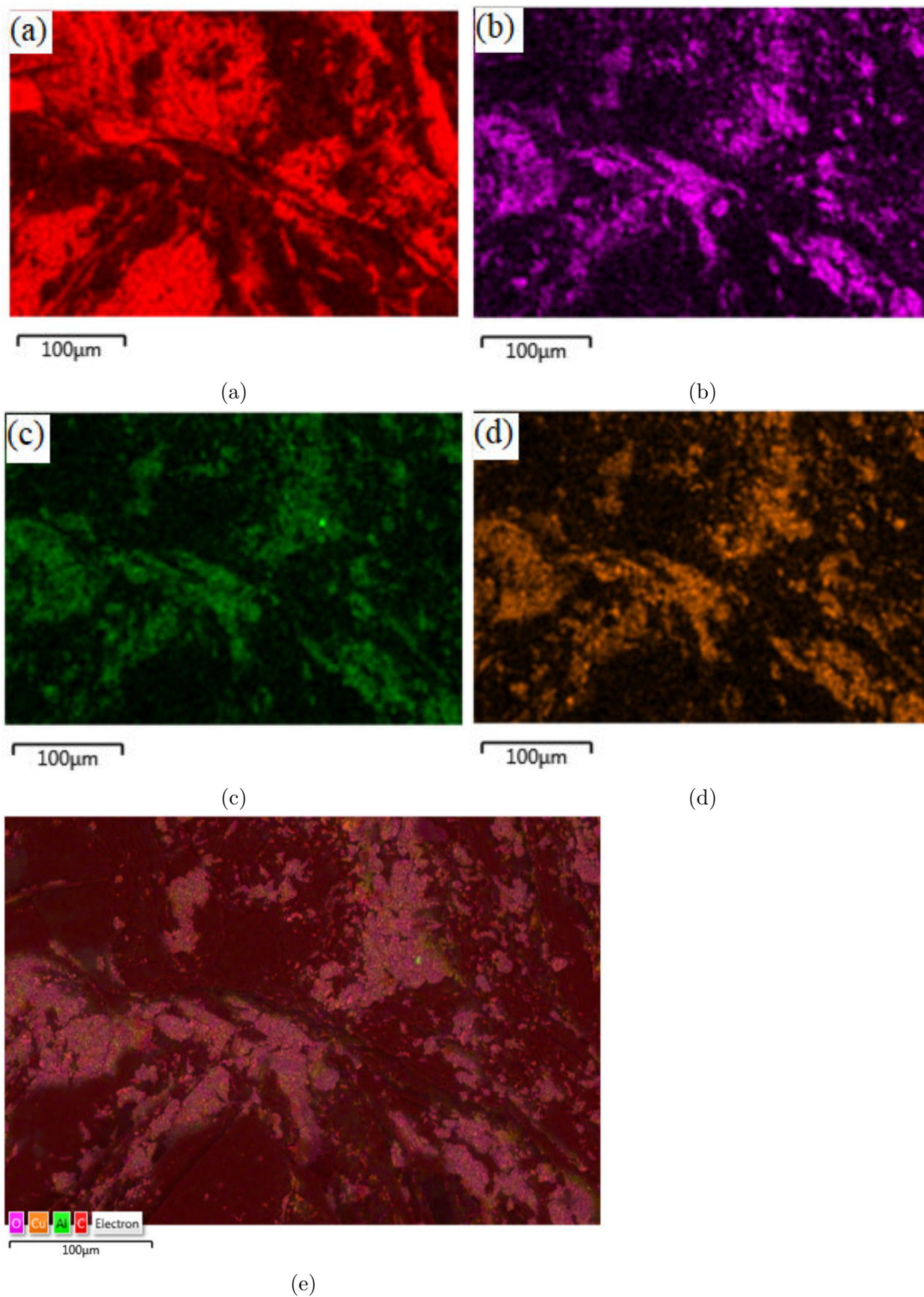
Figure 4: *EDX mapping of RT–28HC/$Al_2O_3$+CuO hybrid NePCM: (a)-Carbon (red), (b)-Oxygen (purple), (c)-Aluminium (green), (d)-Copper (Brown), and (e)-EDX map of oxygen, copper, aluminium, and carbon elements present in RT–28HC/$Al_2O_3$+CuO.*
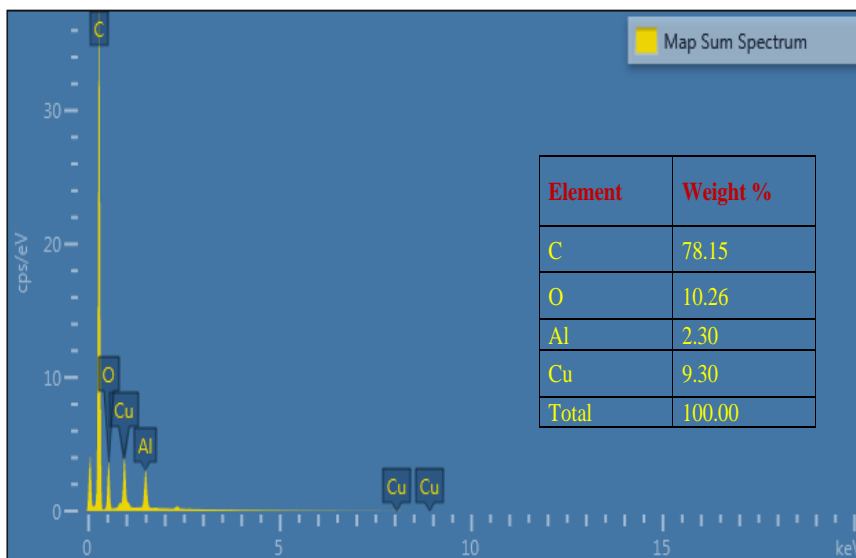
Figure 5: *Elemental spectrum and compositional analysis of RT–28HC/Al₂O₃+CuO.*
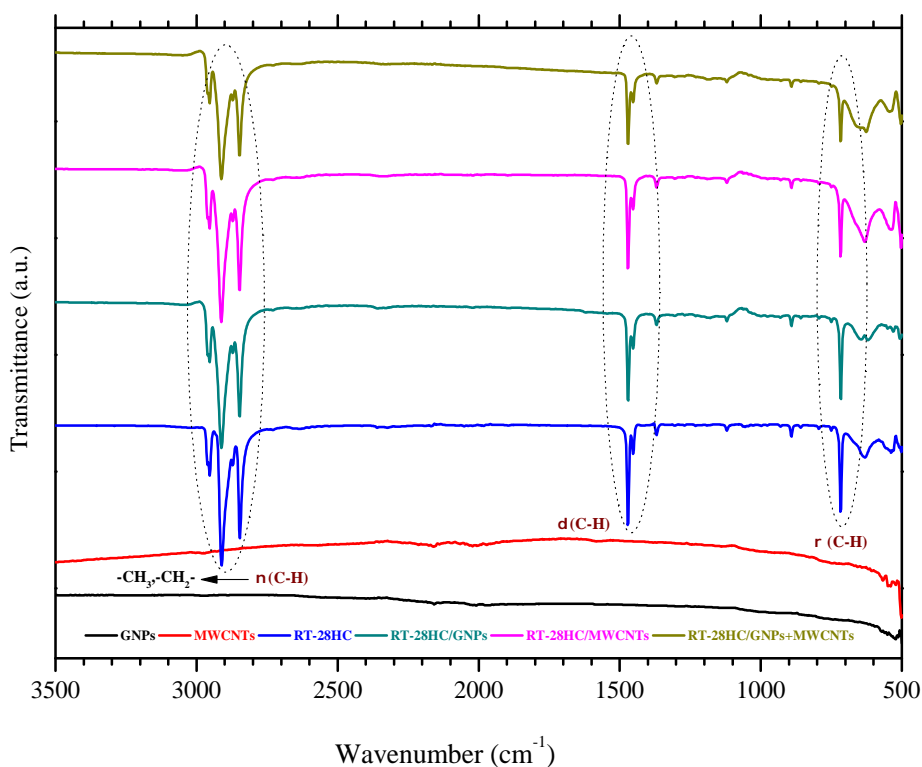


Figure 6: *FT–IR spectrum of GNPs, MWCNT, RT–28HC based mono and hybrid NePCMs.*

spectra of NePCMs have previously been observed [39, 57, 58].

### 3.3. XRD analysis

To analyse the crystal structure of the carbon-based and metallic oxide-based NePCMs, especially in the crystalline phase, XRD spectrum were identified and compared with the data retrieved from the International Centre for Diffraction Data (ICDD), as shown in Figures 8 and 9, respectively. The XRD peaks confirmed the presence of MWCNTs, GNP,
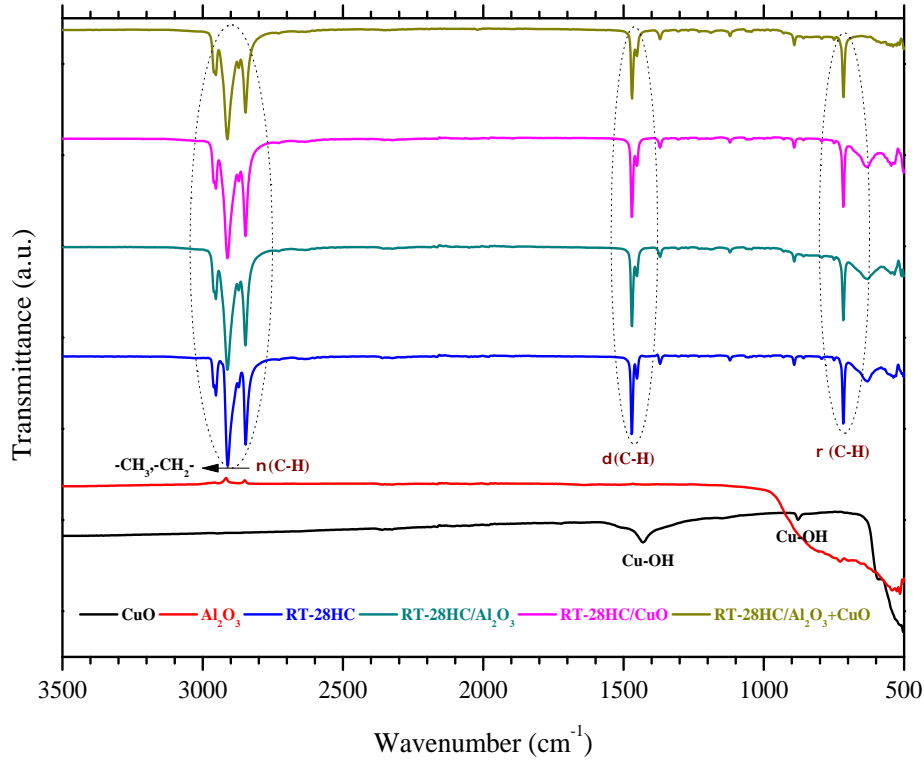
Figure 7: *FT–IR spectrum of CuO, Al$_2$O$_3$, RT–28HC based mono and hybrid NePCMs.*

Al$_2$O$_3$ and CuO nanoparticles in RT–28HC. Figure 8 shows the crystal structure XRD spectrum of MWCNTs, GNPs, mono (RT–28HC/GNPs and RT–28HC/MWCNTs) and hybrid NePCM (RT–28HC/GNPs+MWCNTs). The diffraction peaks of $2\theta$ at 25.91° (002) and 42.95° (100) confirmed the carbon nanotubes with the PDF No. 00–058–1638 [59]. The XRD sharp peaks of GNPs at 26.54°, 42.36°, 44.56° and 54.66° correspond to the planes of (002), (100), (101) and (004), respectively, of graphene layers with PDF No. 00–056–0159. The XRD patterns of both MWCNTs and GNPs can be seen in Figure 8. The comparisons of XRD peaks of Al$_2$O$_3$ confirmed the presence of $\gamma-$phase of Al$_2$O$_3$ nanoparticles of $2\theta$ at 19.50° (013), 32.80° (022), 34.60° (117), 36.76° (122), 39.50° (026) and 45.64° (220) with PDF No. 00–046–1131. The diffraction peaks of CuO at 32.50° (110), 35.54° (111), 38.70° (111), 46.26° (112), 48.71° (202), 53.48° (020), and 58.26° (202) with PDF No. 01–073–6023 [60]. The XRD peaks of Al$_2$O$_3$ and CuO are shown in Figure 9. The sharp diffraction peaks of pure RT–28HC at $2\theta = 7.67°, 11.49°, 15.37°, 19.25°, 19.75°, 22.20°, 23.35°, 24.75°,$ 27.09°, 31.02°, 35.00°, 39.64° and 44.64° are attributed to the crystal planes of $n-Octadecane$ (C$_{18}$H$_{38}$) at (002), (003), (004), (010), (011), (401), (102), (111), (007), (008), (009), (122) and (0110), respectively, with PDF No. 00–053–1532. Since the mass fraction, 1.0 wt.%, is a very small amount of nanoparticles (MWCNTs, GNPs, Al$_2$O$_3$ and CuO) dispersed in RT–28HC, less significant physical changes in the mono and hybrid NePCMs are observed.

16

Thus, XRD patterns reveals that crystal formation of RT–28HC did not alter and both mono and hybrid NePCMs contains the peaks of GNPs, MWCNTs, $Al_2O_3$ and CuO.
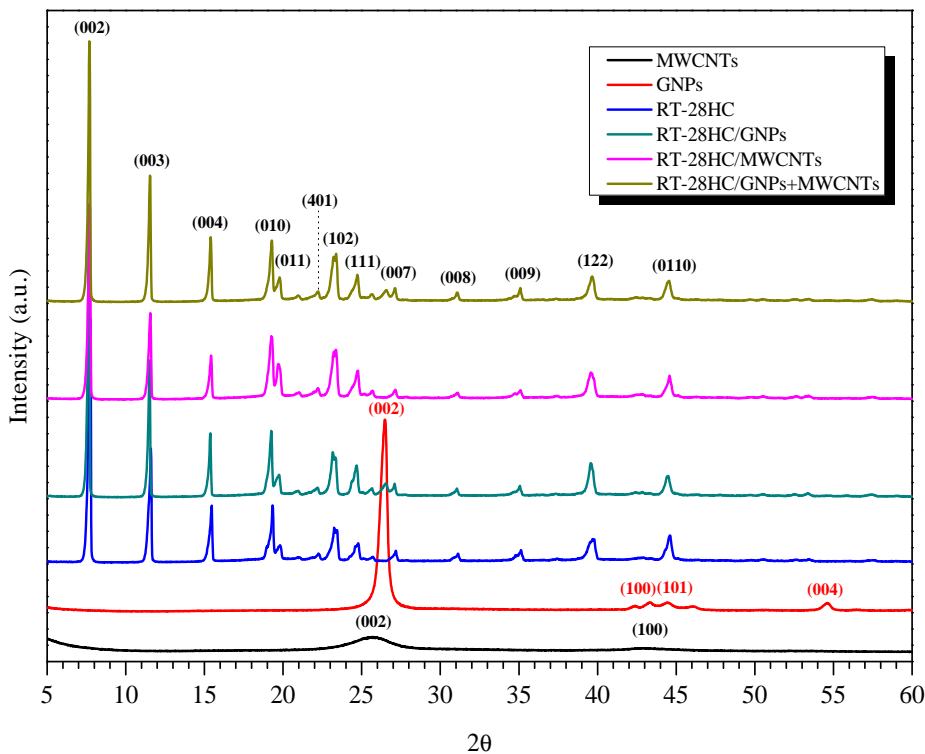


Figure 8: *XRD pattern of GNPs, MWCNT, RT–28HC based mono and hybrid NePCMs.*
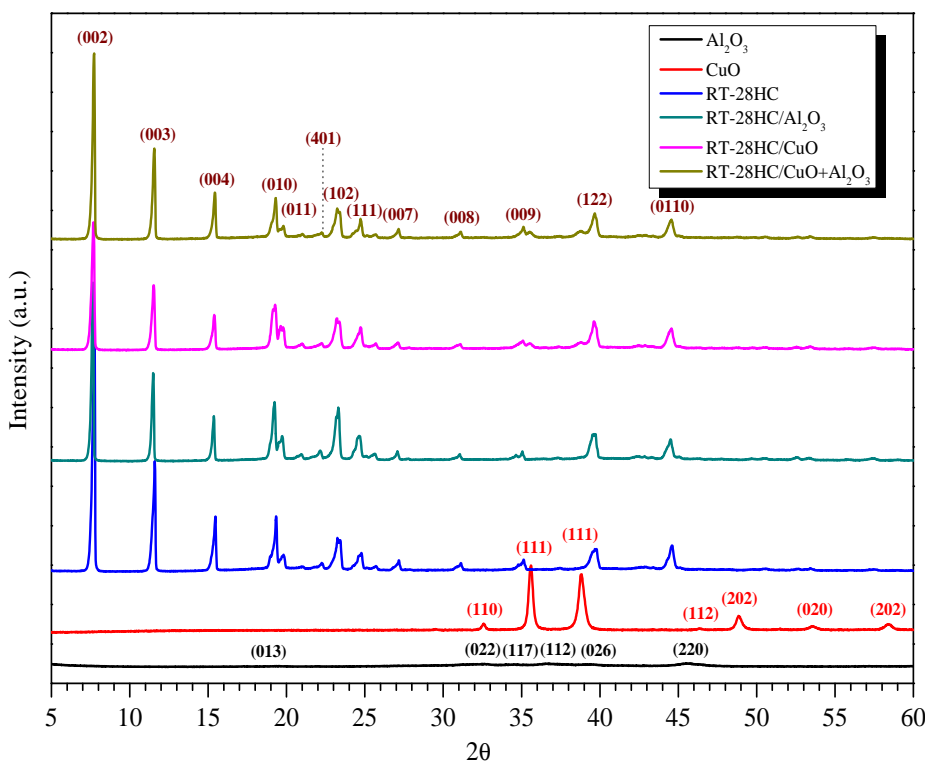


Figure 9: *XRD pattern of CuO, $Al_2O_3$, RT–28HC based mono and hybrid NePCMs.*

## 3.4. TGA and DTG analysis

Thermal stability of pure and hybrid NePCMs were performed by conducting TGA and DTG analysis. The thermal stability is estimated based on the onset temperature of PCM degradation and the weight loss rate at which it occurs. A one–step thermal degradation process can be seen for NePCMs from TGA curves as it happens continuously. However, a two–step can be observed in DTA curves. The TGA and DTG curves of carbon–based (GNPs and MWCNTs) and metallic oxide–based (CuO and $Al_2O_3$) NePCMs are presented in Figure 10 and 11, respectively. From TGA curves it can be seen that there is no perceptible weight loss up to $\sim 120°C$ for all mono and hybrid NePCMs samples. However, the weight loss appeared onward when the temperature increased and rate of the weight loss increased with the increase of the temperature. The TGA curve shows from Figure 10a that RT–28HC starts decomposing from a temperature of 193.73°C until maximum–rate degradation temperature at 230.95°C, with a remaining charred residue of 0.65%. This complete decomposition is caused by the evaporation of RT–28HC, in which hydrocarbon chains breakdown into monomers. In the case of hybrid NePCM (RT–28HC/GNPs+MWCNTs), there no change in weight loss was observed at 120°C, with the onset decomposition temperature and maximum-rate degradation temperature at 203.91°C and 241.70°C, respectively, with a charred residue of 1.68%. Similarly, the onset decomposition and maximum–rate degradation temperature were 205.14°C and 242.53°C, respectively, for RT–28HC/$Al_2O_3$+CuO, as shown in Figure 11a. Since the mass concentration of GNPs, MWCMTs, $Al_2O_3$, CuO, GNPs+MWCNTs and $Al_2O_3$+CuO is much less in RT–28HC, so these carbon–based and metallic oxide–based additives had only a small effect on thermal stability. In NePCMs, the GNPs, MWCNTs, $Al_2O_3$ and CuO layers create a protective layer on the surface of RT–28HC, which delays vaporization of RT–28HC during the thermal degradation. As nanoparticles are likely to sediment which effect the thermal properties, the constant amount of 1.0 wt.% of nanoparticles has a small variation in temperature change during the weight loss. The DTG curves of mono and hybrid NePCMs shown in Figure 10b and 11b confirm that the dispersion of nanoparticles enhance the thermal stability of RT–28HC. The onset decomposition and maximum degradation temperatures of all samples are summarized in Table 2. Since no decompositions in materials have been observed until 120°C, hybrid NePCMs can effectively be used for thermal management of electronic devices.
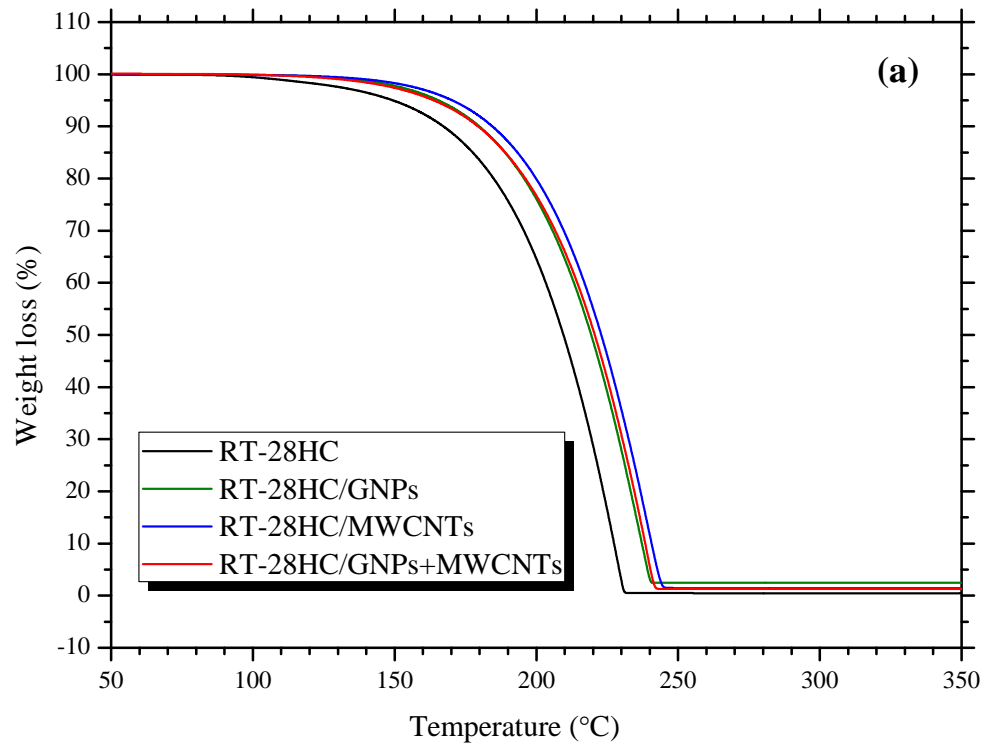
(a)
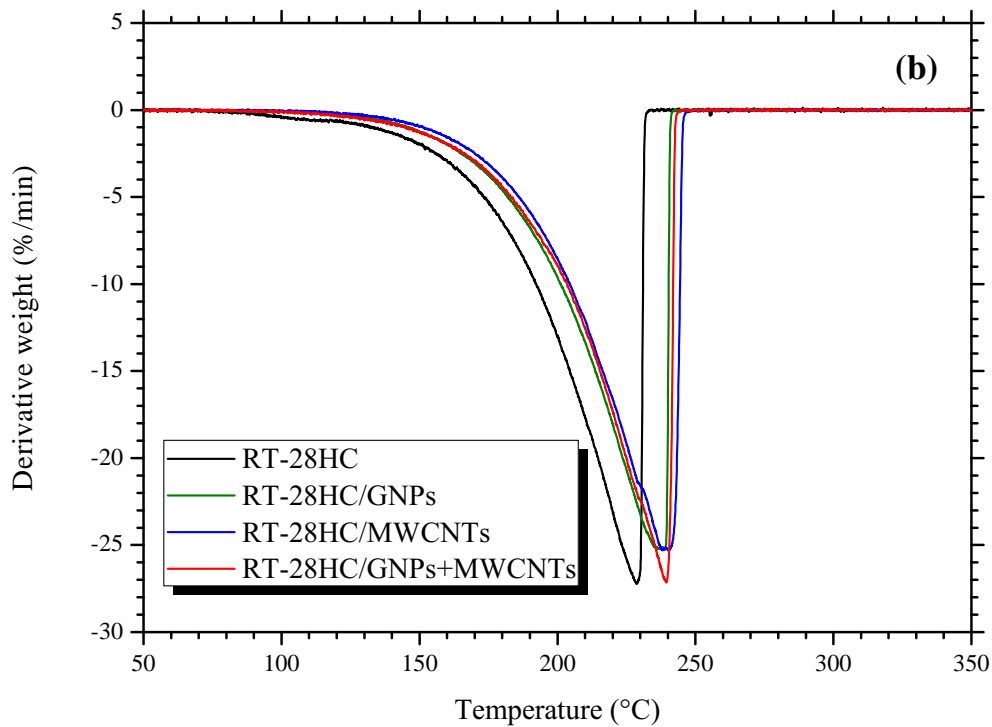


(b)

Figure 10: *(a)-TGA and (b)-DTG thermograms of carbon–based mono and hybrid NePCMs.*

## 3.5. DSC analysis

Phase–change properties, such as phase change temperatures and latent-heats during melting and solidification of pure RT–28HC and NePCMs, have been investigated using
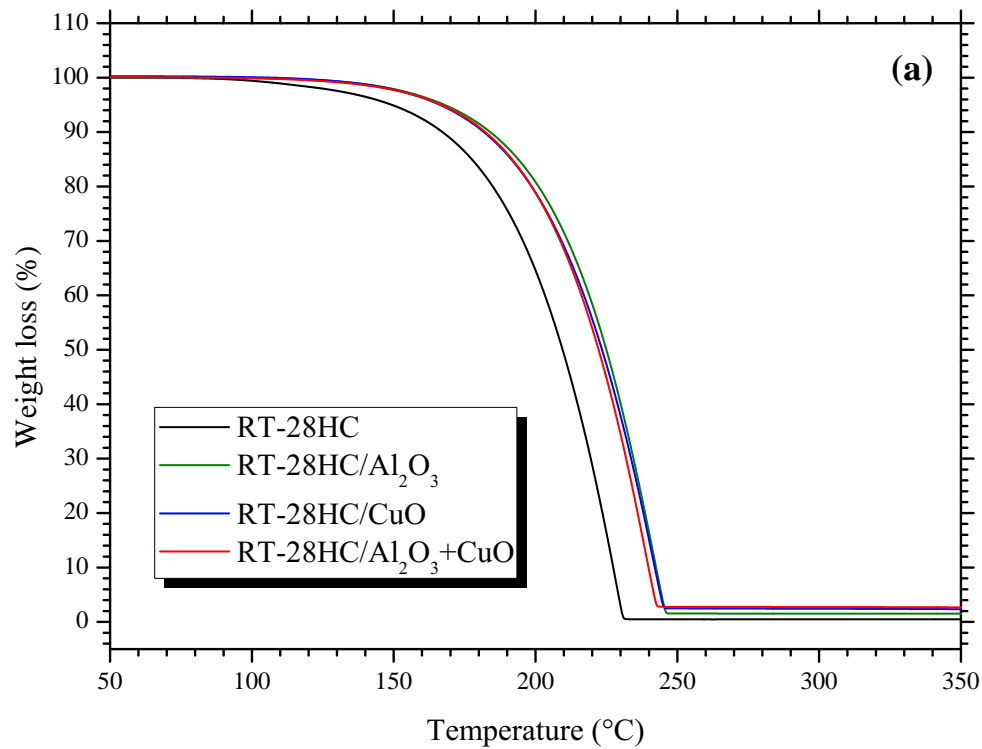
(a)
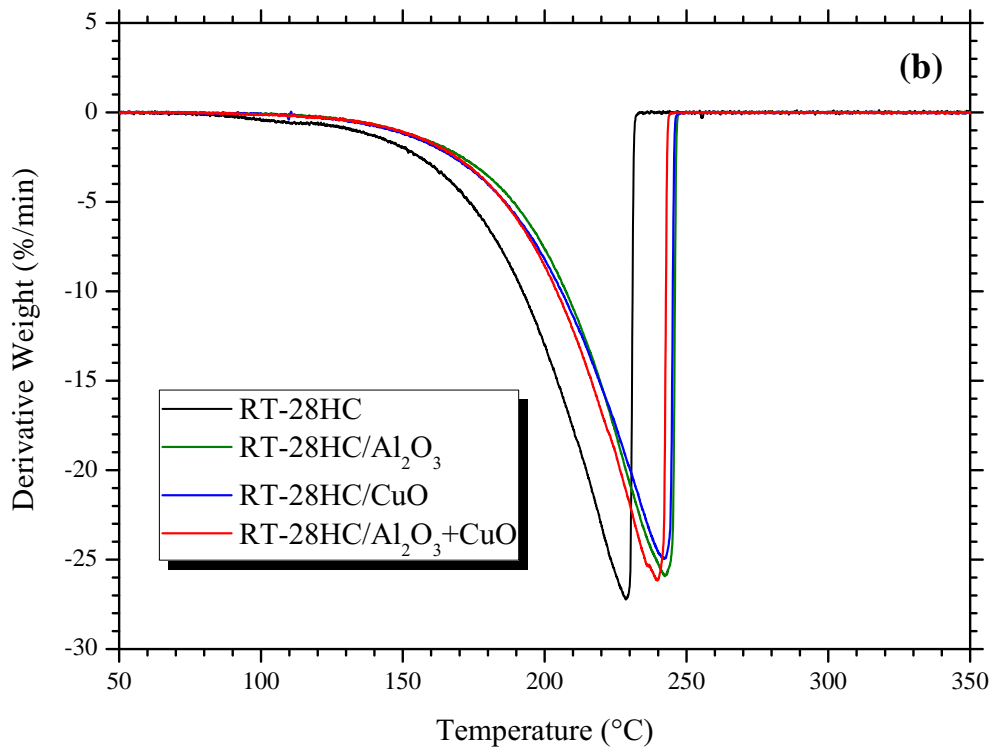


(b)

Figure 11: *(a)-TGA and (b)-DTG thermograms of carbon–based metallic oxide–based mono and hybrid NePCMs.*

DSC. Figure 12 and 13 illustrate DSC measurements of carbon–based and metallic oxide–based nanoparticles NePCMs, respectively, during the melting process. The measured val-

Table 2: *Decomposition temperatures and residue of mono and hybrid NePCMs.*

| Sample | Onset decomposition temperature (°C) | Maximum–rate degradation temperature (°C) | Residue (%) |
|---|---|---|---|
| RT–28HC | 193.73 | 230.95 | 0.65 |
| RT-28HC/GNPs | 201.45 | 240.22 | 2.71 |
| RT-28HC/MWCNTs | 205.11 | 244.06 | 2.17 |
| RT-28HC/GNPs+MWCNTs | 203.91 | 241.70 | 1.68 |
| RT-28HC/$Al_2O_3$ | 207.48 | 245.80 | 2.32 |
| RT-28HC/CuO | 205.19 | 244.98 | 2.73 |
| RT-28HC/$Al_2O_3$+CuO | 205.14 | 242.53 | 3.61 |

ues of corresponding thermal properties are summarized in Table 3. It can be seen that the addition of nanoparticles (GNPs, MWCNT, $Al_2O_3$ and CuO) have slightly affected the thermal properties. In addition, the latent heat of melting and solidification of all mono and hybrid NePCMs were decreased with the addition of GNPs, MWCNT,$Al_2O_3$ and CuO as expected. The maximum reduction in melting latent–heats of RT–28HC/GNPs, RT–28HC/MWCNTs and RT–28HC/GNPs+MWCNTs have been found to be 2.37%, 2.56% and 3.75%, respectively, as compared to the pure RT–28HC. Similarly, the maximum reduction in solidification latent–heats are 2.83%, 2.85%, 3.54% for RT–28HC/GNPs, RT–28HC/MWCNTs and RT–28HC/GNPs+MWCNTs, respectively. The maximum reduction in latent–heats of melting are 2.14%, 3.02% and 2.44% for RT–28HC/$Al_2O_3$, RT–28HC/CuO and RT–28HC/$Al_2O_3$+CuO, respectively. In addition, the maximum reduction in solidification latent–heats are 2.26%, 2.92% and 2.61% for RT–28HC/$Al_2O_3$, RT–28HC/CuO and RT–28HC/$Al_2O_3$+CuO, respectively. Single endothermic peaks are observed during the melting of RT–28HC and NePCMs samples, indicating an isomorphous crystalline form of RT–28HC either in a pristine state or in the NePCMs one. Whereas, a bimodal crystallization exothermic peaks are observed by RT–28HC and NePCMs samples. Normally, the cooling curve of the n–Alkanes is divided into three sections of crystallization peaks, alpha ($\alpha$), beta ($\beta$) and gamma ($\gamma$). On the DSC cooling curve, the exothermic $\alpha-$peak corresponds to the heterogeneously nucleated liquid–rotator transition, the $\beta-$peak is attributed to the homogeneously nucleated rotator-crystal transition, and the $\gamma-$peak corresponds to the heterogeneously nucleated liquid–crystal transition. Further, $\alpha-$peak appears a high shoulder at higher temperature than the -peak which appears at low temperature shoulder. Whereas, $\gamma-$peak forms the highest peak than the $\alpha$ and $\beta$ peaks but at lower temperature compared to $\alpha$ and $\beta$ peaks while cooling process. This means that more than 80% of the latent heat is released at the lower temperature due the formation of $\gamma-$peak in n–Alkanes [61]. In addition, the shoulder height of each peak further depends on the cooling rate of n–Alkanes. The literature has reported that with the increase of heating and cooling rate,

21

the only one peak is observed while heating. Whereas, the two or three peaks were observed for all cooling rates [61, 62]. Therefore, the multiple peaks in exothermic process are caused by the difference of cooling rates. While crystallization process at different cooling rates, the crystallization peaks are found to be shifted at higher temperatures and more prominent appearance of $\alpha$, $\beta$ and $\gamma-$peaks are observed with the decrease of cooling rate. Whereas, both onset and peak melting temperatures increase with the increase of heating rate [61, 62, 63]. The bimodal crystallization behaviour with pure PCM and NePCMs is because the formation of crystallization peaks which correspond to different temperatures. During cooling, the PCM and NePCM start solidification from liquid phase and formed a first small $\alpha-$peak at higher temperature at which solidification commences and concludes by forming a metastable rotator phase (liquid–to–rotator transition) as a result of heterogeneous nucleation. A sharp $\gamma-$peak is representing the main exothermic peak, where the rotator phase transformed into a stable triclinic crystalline phase as a result of homogeneous nucleation [64, 65, 66].
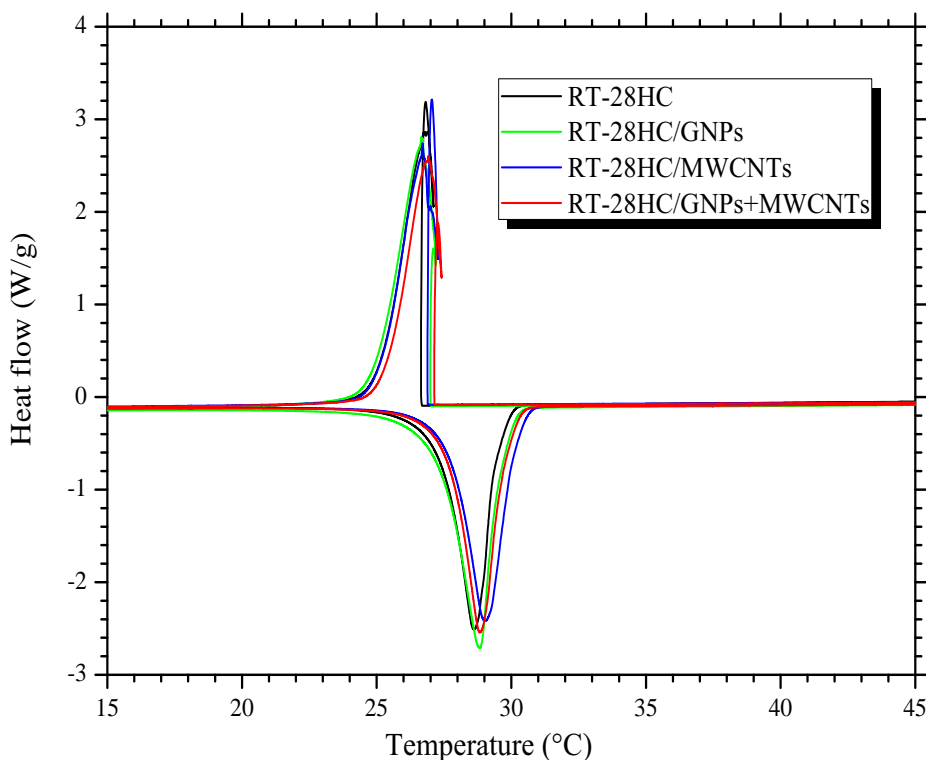


Figure 12: *DSC curves of carbon–based mono and hybrid NePCMs.*

From the DSC results, the comparison of the melting ($\Delta H_m$) and solidification ($\Delta H_s$) enthalpies are presented in Figure 14 and 15 for carbon–based and metallic oxide–based nanoparticles NePCMs, respectively. The $\Delta H_m$ and $\Delta H_s$ of pure RT–28HC was found to be 254.93 and 257.90 J/g, respectively. However, a slight reduction in both can be

22
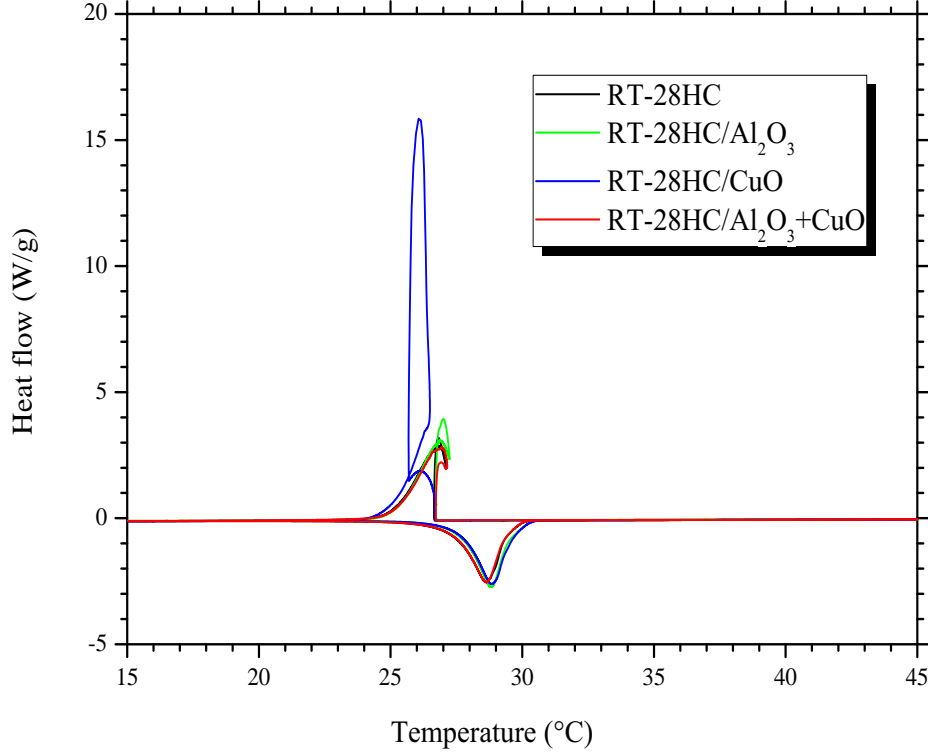
Figure 13: *DSC curves of metallic oxide–based mono and hybrid NePCMs.*

374  observed for NePCMs which is due to the introduction of GNPs, MWCNTs, Al$_2$O$_3$ and CuO

375  nanoparticles. The mass fraction ($\omega$) of crystallized RT–28HC in NePCMs is determined

376  by Equation 1:

$$\omega = \frac{\Delta H_{NePCM}}{\Delta H_{PCM}} \times 100 \tag{1}$$

377  where, $\Delta H_{NePCM}$ and $\Delta H_{PCM}$ are the endothermic latent–heat of NePCMs and pure PCM,

378  respectively.

379      The degree of super–cooling ($\Delta T$) of NePCMs are shown in Figure 16 and 17 for carbon–

380  based and metallic oxide–based nanoparticles NePCMs, respectively. The peak melting

381  temperature (T$_m$) and crystallization temperature (T$_c$) of RT–28HC were found to be

382  28.89°C and 26.80°C, respectively. The maximum deviations in T$_m$ and T$_c$ are determined as

383  $-0.28\%$ and $-0.60\%$ for RT–28HC/GNPs, $-0.24\%$ and $-0.93\%$ for RT–28HC/MWCNTs,

384  and $-0.17\%$ and $-0.78\%$ for RT–28HC/GNPs+MWCNTs, respectively, compared to RT–

385  28HC. Similarly, the maximum deviations in T$_m$ and T$_c$ are $-0.03\%$ and $-0.78\%$ for RT–

386  28HC/Al$_2$O$_3$, $-0.17\%$ and $-0.56\%$ for RT–28HC/CuO, and $-0.14\%$ and $-0.60\%$ for RT–

387  28HC/Al$_2$O$_3$+CuO, respectively. The reduction in $\Delta T$ for hybrid NePCMs are found to

388  be 1.93°C and 1.97°C for RT–28HC/GNPs+MWCNTs and RT–28HC/Al$_2$O$_3$+CuO, respec-
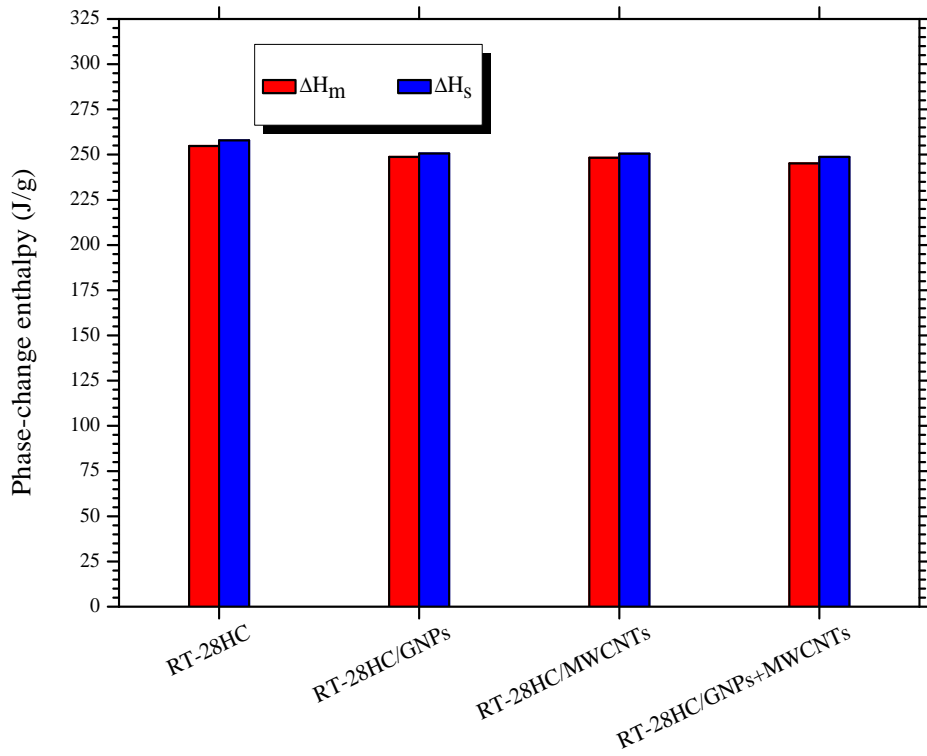
Figure 14: *Phase change enthalpies of carbon–based mono and hybrid NePCMs.*
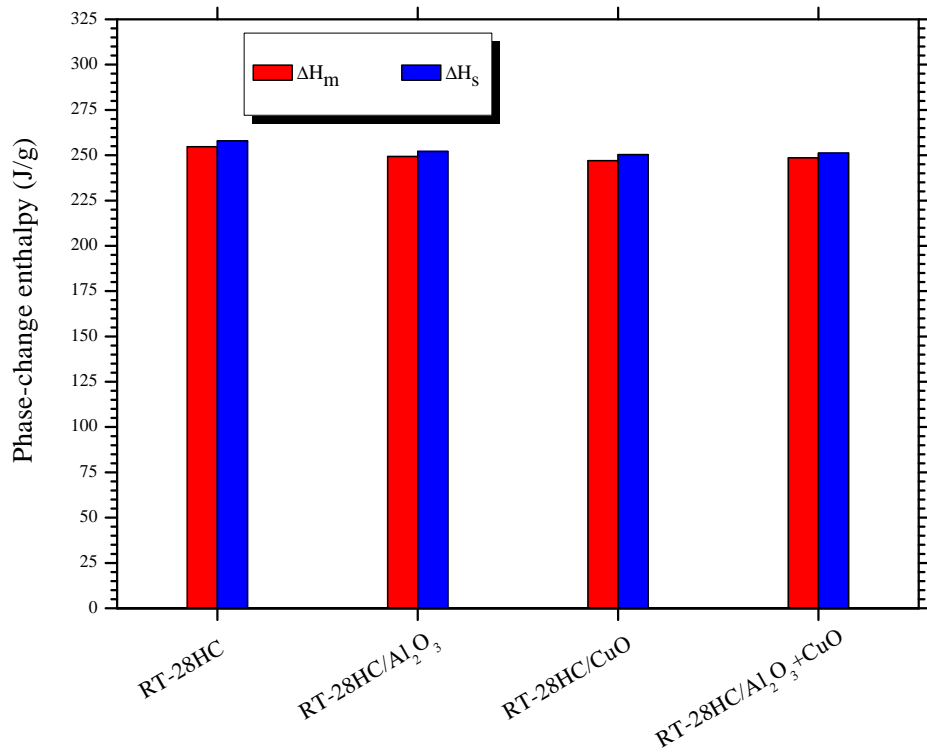


Figure 15: *Phase change enthalpies of metallic oxide–based mono and hybrid NePCMs.*

tively, which demonstrates the more signified role of GNPs+MWCNTs as nucleating agents compared with $Al_2O_3$+CuO in terms of its surface adsorption and effective homogeneous nucleation. Factually, the addition of nanoparticles in RT–28HC, the heterogeneous nucleation

may be favoured at the cost crystallization point depression [67]. It has been extensively reported that a high $\Delta T$ is evidently disadvantageous for utilization of PCM in thermal management because it can result in a hysteresis response to heat transfer.
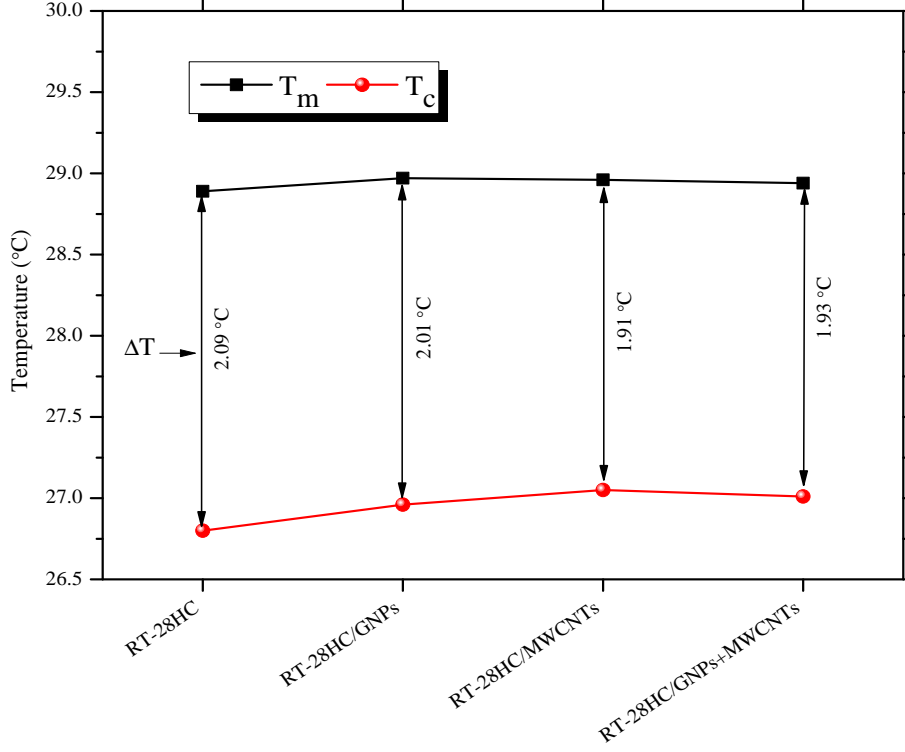


Figure 16: *Degree of super–cooling of carbon–based mono and hybrid NePCMs.*

Figure 18 and 19 illustrate the experimental and calculated latent-heat of fusion for NePCMs, which can be calculated from Equation 2 [68]:

$$\Delta L_{NePCM} = \Delta L_{PCM} \cdot \omega = \Delta L_{PCM}(1 - \varphi) \tag{2}$$

where, $\Delta L_{NePCM}$ represents the calculated latent–heat of fusion of NePCM, $\Delta L_{PCM}$ represents the latent heat of pure PCM, and $\omega$ and $\varphi$ are the mass fraction of pure PCM and nanoparticles, respectively.

It can be observed from Figure 18 and 19 that the experimentally measured latent–heat of fusion for each NePCM is lower than that of the calculated value. The deviation in values is based on the type of nanoparticles, as the mass fraction of all the nanoparticles is constant 1.0 wt.%. Similar deviations in experimental and calculated values have been reported in the investigations of Li et al. [30], Sharma et al. [39], Tian et al. [68] and Wang et al. [69]. In addition, a relative error of 2.78% and 1.46% are obtained between the calculated and experimental values of RT–28HC/GNPs+MWCNTs and RT–28HC/Al$_2$O$_3$+CuO, respec-
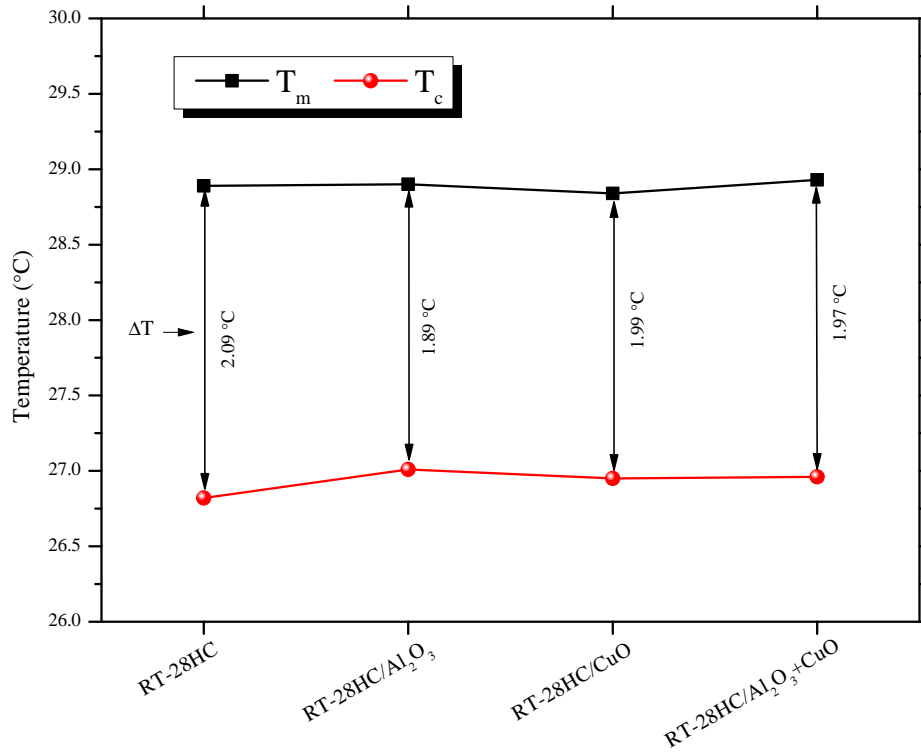
Figure 17: *Degree of super–cooling of metallic oxide–based mono and hybrid NePCMs.*

tively, with the hybrid NePCMs having latent–heat fusion of 245.18 J/g and 248.51 J/g, respectively. The results show that the hybrid NePCM of RT–28HC/GNPs+MWCNTs at 1.0 wt.% has the optimum value of latent heats, which is favourable for thermal management applications. The decrease in latent–heats results in the increase of thermal conductivity. Furthermore, the discrepancies in the calculated values may be due the surface morphology, structure, size and rate of dispersion of nanoparticles in RT–28HC.
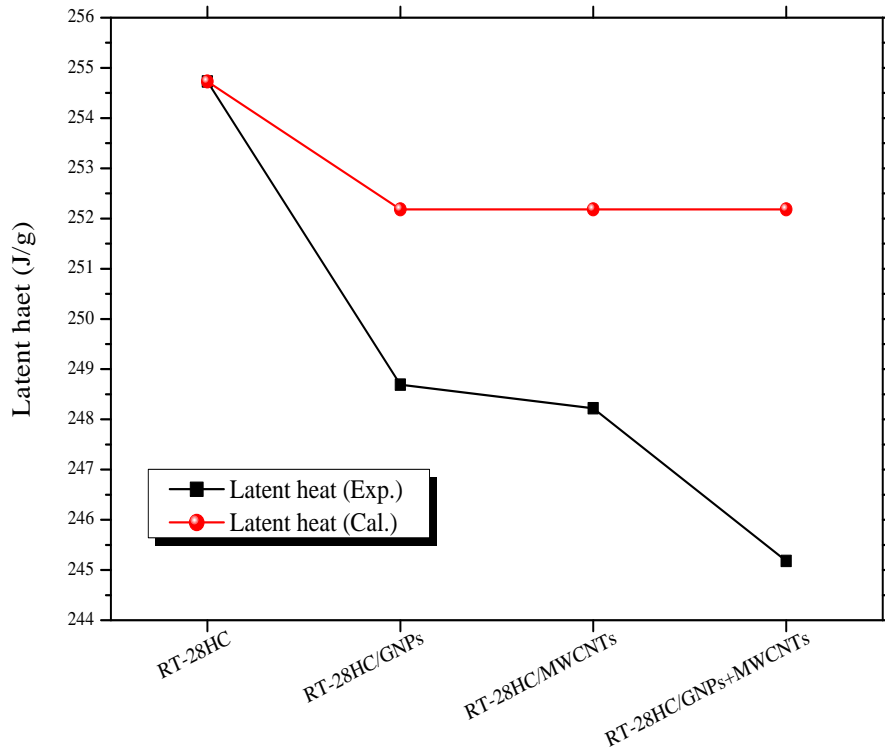
Figure 18: *Comparison of latent heats of carbon–based mono and hybrid NePCMs.*
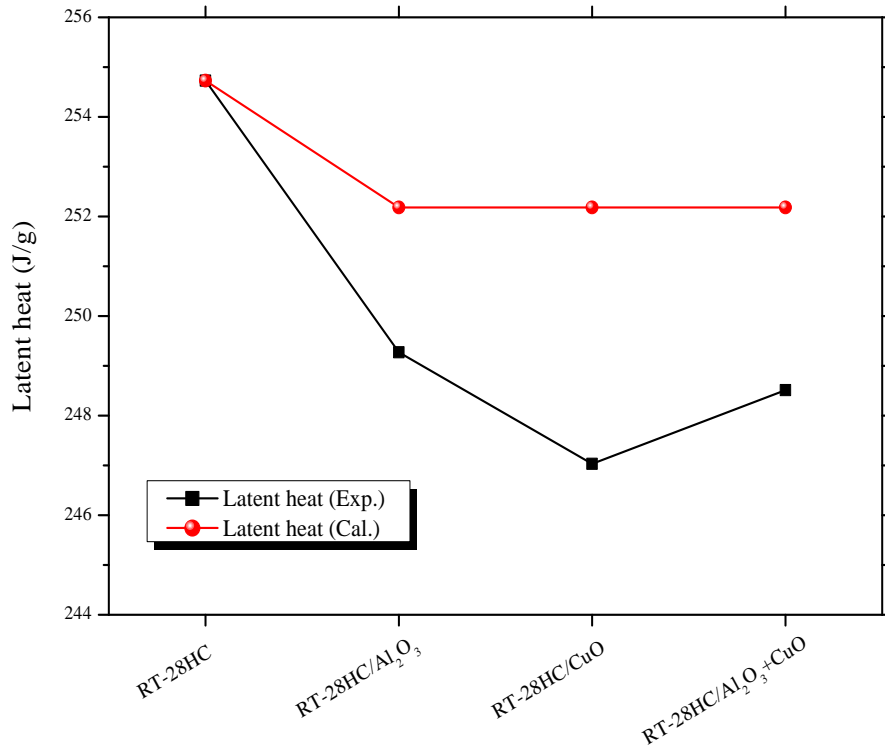


Figure 19: *Comparison of latent heats of metallic oxide–based mono and hybrid NePCMs.*

Table 3: *Phase-change properties of mono and hybrid NePCMs\*.*

| Sample | Melting | | | | | Solidification | | | | | $\omega$ (%) | $\Delta T$ |
|---|---|---|---|---|---|---|---|---|---|---|---|---|
| | $T_{oset,m}$ | $T_{peak,m}$ | $\Delta H_{m,exp}$ | $\Delta H_{m,cal}$ | RE (%) | $T_{oset,c}$ | $T_{peak,c}$ | $\Delta H_{c,exp}$ | $\Delta H_{c,cal}$ | RE (%) | | |
| RT–28HC | 27.38 | 28.89 | 254.73 | – | – | 26.64 | 26.80 | 257.90 | – | – | 100 | 2.09 |
| RT–28HC/GNPs | 27.40 | 28.97 | 248.69 | 252.18 | 1.38 | 26.98 | 26.66 | 250.61 | 255.32 | 1.85 | 97.63 | 2.01 |
| RT–28HC/MWCNTs | 27.70 | 28.96 | 248.22 | 252.18 | 1.57 | 26.89 | 27.05 | 250.55 | 255.32 | 1.87 | 97.44 | 1.91 |
| RT–28HC/GNPs+MWCNTs | 27.60 | 28.94 | 245.18 | 252.18 | 2.78 | 27.13 | 27.01 | 248.77 | 255.32 | 2.57 | 97.44 | 1.93 |
| RT–28HC/Al$_2$O$_3$ | 27.63 | 28.90 | 249.27 | 252.18 | 1.15 | 26.72 | 27.01 | 252.08 | 255.32 | 1.27 | 97.86 | 1.89 |
| RT–28HC/CuO | 27.64 | 28.94 | 247.03 | 252.18 | 2.04 | 25.65 | 26.95 | 250.36 | 255.32 | 1.94 | 96.98 | 1.99 |
| RT–28HC/Al$_2$O$_3$+CuO | 27.37 | 28.93 | 248.51 | 252.18 | 1.46 | 26.71 | 26.96 | 251.18 | 255.32 | 1.62 | 97.56 | 1.97 |

\* $T_{oset,m}$ : onset melting temperature, $T_{peak,m}$ : peak melting temperature, $\Delta H_{m,exp}$: experimental latent-heat of melting,

$\Delta H_{m,cal}$ : calculated latent-heat of melting, $T_{oset,c}$ : onset solidifying temperature, $T_{peak,c}$ : peak solidifying temperature,

$\Delta H_{c,exp}$ : experimental latent-heat of solidifying, $\Delta H_{c,cal}$ : calculated latent-heat of solidifying, RE: relative error,

$\omega$: Mass percentage of RT–35HC, $\Delta T$: Degree of supercooling

### 3.6. Thermal conductivity analysis

The primary function of PCM in thermal management application is to absorb and release the thermal energy while melting and solidifying effectively. The rate of thermal energy storage and release during fusion and crystallization is highly dependent on the thermal conductivity of the PCM. The low thermal conductivity of the pure PCMs reduces both the rate of heat storage and release and restrict its applications. A PCM with higher thermal conductivity increases the heat transfer rate during melting and solidification processes, which in turn reduces the melting and solidification time [1]. Figure 20 presents the thermal conductivities of pure RT–28HC, RT–28HC/GNPs, RT–28HC/MWCNTs and RT–28HC/GNPs+MWCNTs. Similarly, Figure 21 presents the thermal conductivities of pure RT–28HC, RT–28HC/$Al_2O_3$, RT–28HC/CuO and RT–28HC/$Al_2O_3$+CuO. The thermal conductivities of RT–28HC dispersed with carbon–based and metallic oxides–based nanoparticles are measured at temperature of 20°C and 25°C for solid–phase and 30-45°C for liquid–phase with an increment of 5°C. It can observed from Figure 20 and 21 that thermal conductivity generally increases with the addition of nanoparticles, which is due to the higher thermal conductivity of nanoparticles compared to the pure PCM. The higher thermal conductivities were obtained for pure RT–28HC and NePCMs at temperature of 20°C and 25°C in solid–phase. Contrarily, the lower thermal conductivity values were observed in liquid–phase at temperature range from 30°C to 45°C. This reveals that the thermal conductivity is strongly dependent on temperature. This decreasing trend in thermal conductivity of pure RT–28HC and NePCMs with temperature is because of the turning of the orderly microstructure of pure RT–28HC in solid–phase into disorderly microstructure in liquid-phase. In solids, the heat is conducted by lattice vibrations as the molecules vibrate within their lattice structure. This lattice vibration and motion of free electron are the most efficient in solids than liquids. Therefore solids generally possess the higher thermal conductivity than liquids. Thermal conductivities of 0.378, 0.355 and 0.430 W/m.K were obtained for RT–28HC/GNPs, RT–28HC/MWCNTs and RT–28HC/GNPs+MWCNTs, respectively at 20°C, as shown in Figure 20. Thermal conductivities of RT–28HC/$Al_2O_3$, RT–28HC/CuO and RT–28HC/$Al_2O_3$+CuO were 0.318, 0.332 and 0.328 W/m.K, respectively, at 20°C, as shown in Figure 21. It can be clearly observed that the hybrid NePCM with GNPs+MWCNTs weight percentage of 75%/25% has the highest thermal conductivity among all other mono and hybrid NePCMs.

Figures 22 and 23 illustrate the thermal conductivity enhancement factor of NePCMs
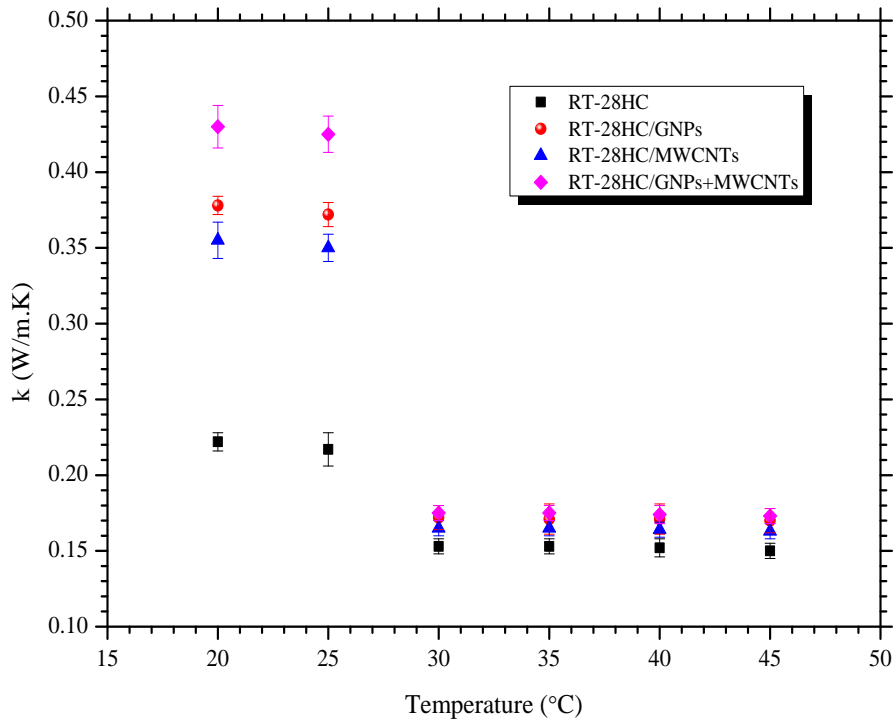
Figure 20: *Thermal conductivity of carbon–based mono and hybrid NePCMs as a function of temperature.*
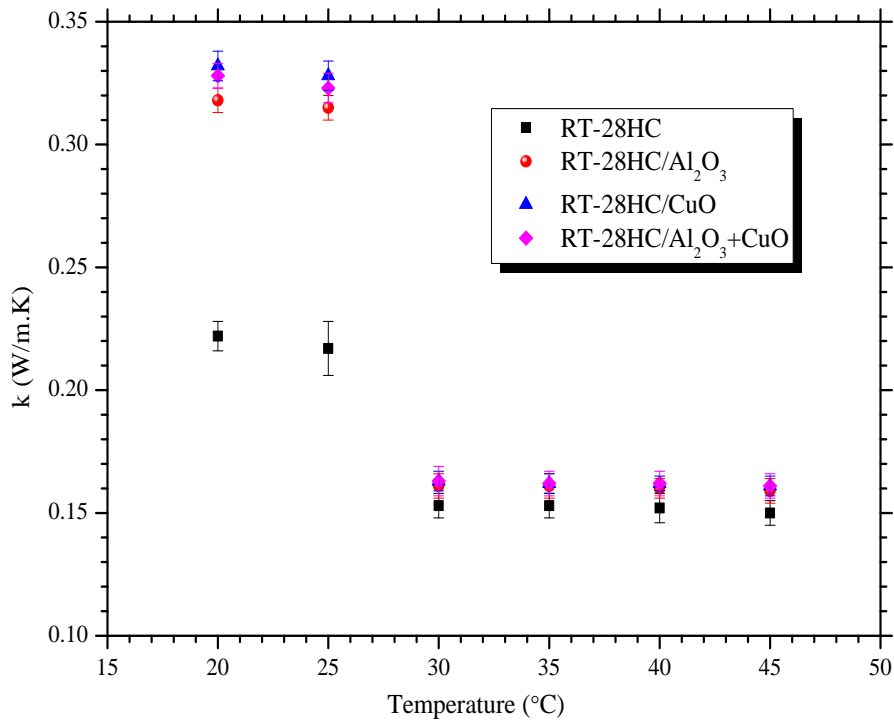


Figure 21: *Thermal conductivity of metallic oxide–based mono and hybrid NePCMs as a function of temperature.*

446  to evaluate the effect of nanoparticles in enhancement of heat transfer rate, as given by

Equation 3:

$$\eta = \frac{k_{NePCM} - k_{PCM}}{k_{PCM}} \times 100 \tag{3}$$

where, $k_{NePCM}$ and $k_{PCM}$ are the thermal conductivity of the NePCM and pure PCM, respectively.

It can be seen from Figures 22 and 23 that the thermal conductivity enhancement increases nonlinearly with respect to temperature for a specific NePCM, either of carbon–based or metallic oxide–based. The relative enhancement in effective thermal conductivity shows that RT–28HC/GNPs+MWCNTs has the higher enhancement of 96% and 94% at 25°C and 20°C, respectively, in solid–phase compared to the RT–28HC/GNPs and RT–28HC/MWCNTs, as shown in Figure 22. The higher thermal conductivity enhancement of RT–28HC/GNPs+MWCNTs is because of the hybrid NePCMs form three–dimensional heat transfer path, which permits transfer of the thermal energy in all regions of the RT–28HC while heating/cooling [22]. A slight decreasing trend can be observed for the case of RT–28HC/Al$_2$O$_3$+CuO hybrid NePCM, which has a maximum thermal conductivity enhancement of 49% and 48% at 25°C and 20°C, respectively, compared to RT–28HC/CuO which has 51% and 50% enhancement in thermal conductivity at 25°C and 20°C, respectively, as shown in Figure 23. The variation in results of RT–28HC/CuO and RT–28HC/Al$_2$O$_3$+CuO is because of the size, morphology, density and dispersion stability of the nanoparticles as well as their inherent thermal conductivity. Since CuO has a higher thermal conductivity than Al$_2$O$_3$, therefore RT–28HC/CuO has a higher thermal conductivity than RT–28HC/Al$_2$O$_3$+CuO having constant mass fraction of 1.0 wt.%. Furthermore, the Al$_2$O$_3$ nanoparticles have the smaller size (13 nm) and density compared to CuO nanoparticles (< 50 nm), which have the better degree of homogenization and rate of dispersion in pure PCM. This reveals the better dispersion stability of hybrid nanoparticles of Al$_2$O$_3$+CuO having mass percentage ratio of 75%/25% dispersed in RT–28HC. In addition, the thermal boundary resistance between the nanoparticles and matrix molecules play a dominant factor for the discrepancy [70]. Furthermore, the results reveal that carbon-based hybrid NePCMs have the much better tendency to store and release the heat rate compared to the metallic oxide based hybrid NePCMs, due to the higher enhancement in thermal conductivity. There are two main factors that enhance the thermal conductance rate of NePCMs. Firstly, the higher thermal conductivity of the nanoparticles and secondly, the motion of the nanoparti-

31

cles in NePCMs in liquid–phase, which causes a quasi–convection phenomenon [36]. Furthermore, the interfacial thermal resistance is reduced with three–dimensional nano-structure as compared to the two–dimensional nano–structure for the case of metallic oxide–based NePCMs between the pure PCM and nanoparticles, which improves the rate of thermal conductance.
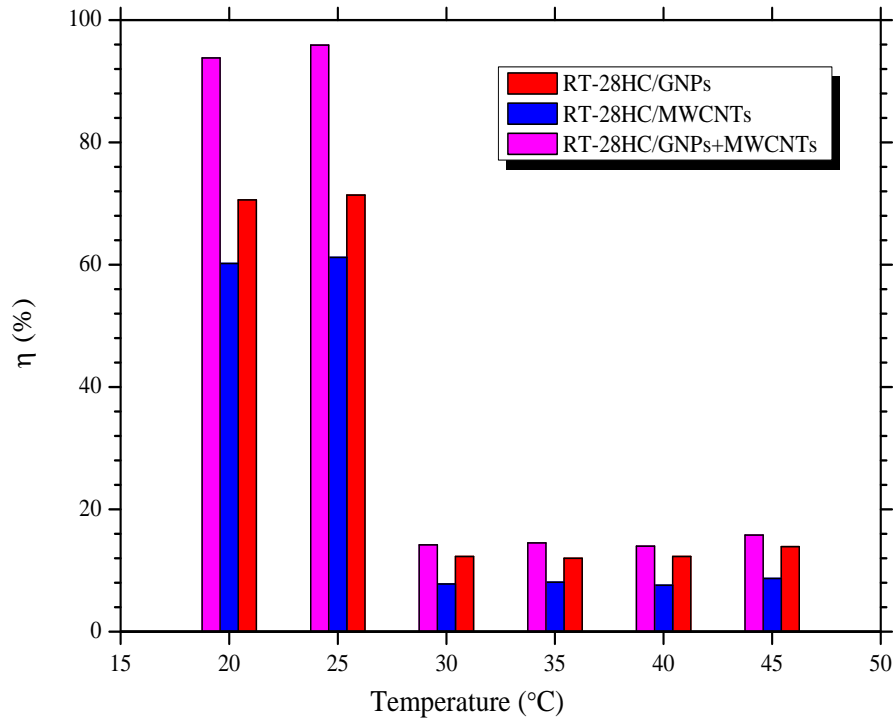


Figure 22: *Thermal conductivity enhancement factor of carbon–based mono and hybrid NePCMs as a function of temperature.*

### 3.7. Infrared thermography (IRT) analysis

Figure 24 illustrates the IR thermographic images of the melting process of RT–28HC, RT–28HC/$Al_2O_3$+CuO and RT–28HC/GNPs+MWCNTs at different time steps from 5 min to 55 min with time step of 5 min. The heating stages of each specimen can be reflected clearing at time step. There is noticeable temperature difference between the background and specimens because of the latent–heat absorption of the specimens during phase–change. The blue colour of the specimens indicates the low temperature, which changes into the red colour during heating indicating the high temperature. The uniform melting of each specimen can be observed while heating, however, the quick flow away and shrinkage is found in pure RT–28HC, shown in Figure 24d. This phase transition from solid–to–liquid causes the pure PCM to lose its shape–stability completely. In the case of hybrid NePCMs specimens, uniform phase transition is observed with slight shrinkage and flow away due to
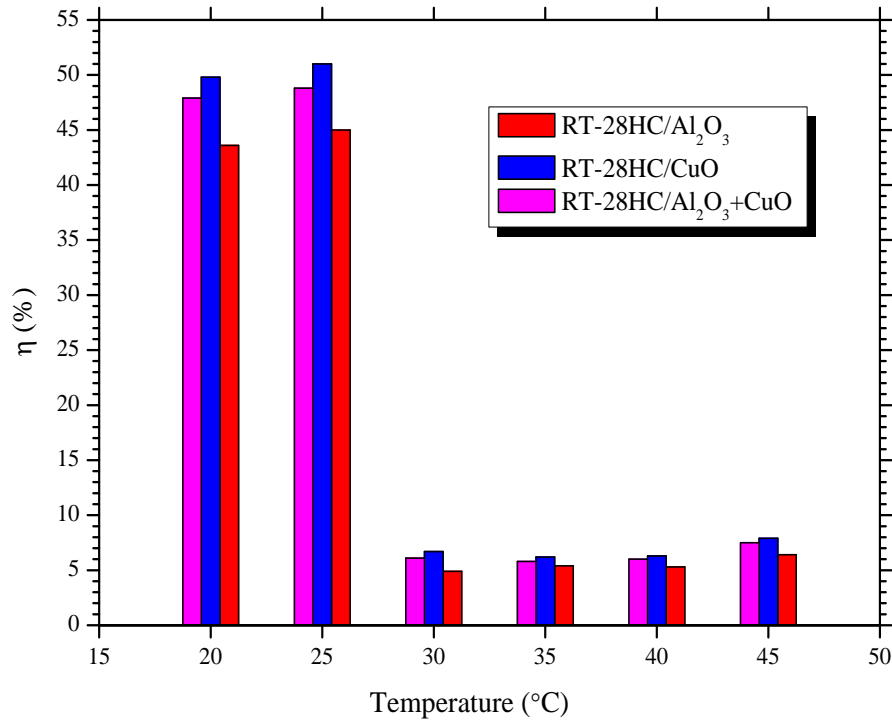
Figure 23: *Thermal conductivity enhancement factor of metallic oxide–based mono and hybrid NePCMs as a function of temperature.*

the heating-impact effect. Since the hybrid NePCMs contain only 1 wt.% of $Al_2O_3+CuO$ and GNPs+MWCNTs, there was therefore only slight shrinkage. However, the shrinkage level and flow away decrease with the increase of the loading of nanoparticles. The melting process of RT–28HC/GNPs+MWCNTs shows there is no complete melting until 50 min and surface temperature is lower than the pure RT–28HC and RT–28HC/$Al_2O_3$+CuO, which reveals the best heat transfer enhancement due the higher thermal conductivity of GNPs and MWCNTs. The enhancement in melting process with GNPs and MWCNTs is due to the uniform and homogenous dispersion of organic based nanoparticles in organic PCMs, which increase the viscosity and shape–stability and lowers the convection heat transfer. The phase transition duration of RT–28HC/GNPs+MWCNTs, compared to pure RT–28HC and RT–28HC/$Al_2O_3$+CuO, improves the heat dissipation rate while thermal management of microelectronics due to constant lower temperature of NePCMs. Furthermore, the results reveal that this enhanced latent heating phase duration and uniform natural convection heat transfer of RT–28HC/GNPs+MWCNTs avoids the overheating and has a greater potential for better thermal management of microelectronics.

33

(a) 5 min       (b) 10 min       (c) 15 min

(d) 20 min       (e) 25 min       (f) 30 min

(g) 35 min       (h) 40 min       (i) 45 min

(j) 50 min       (k) 55 min
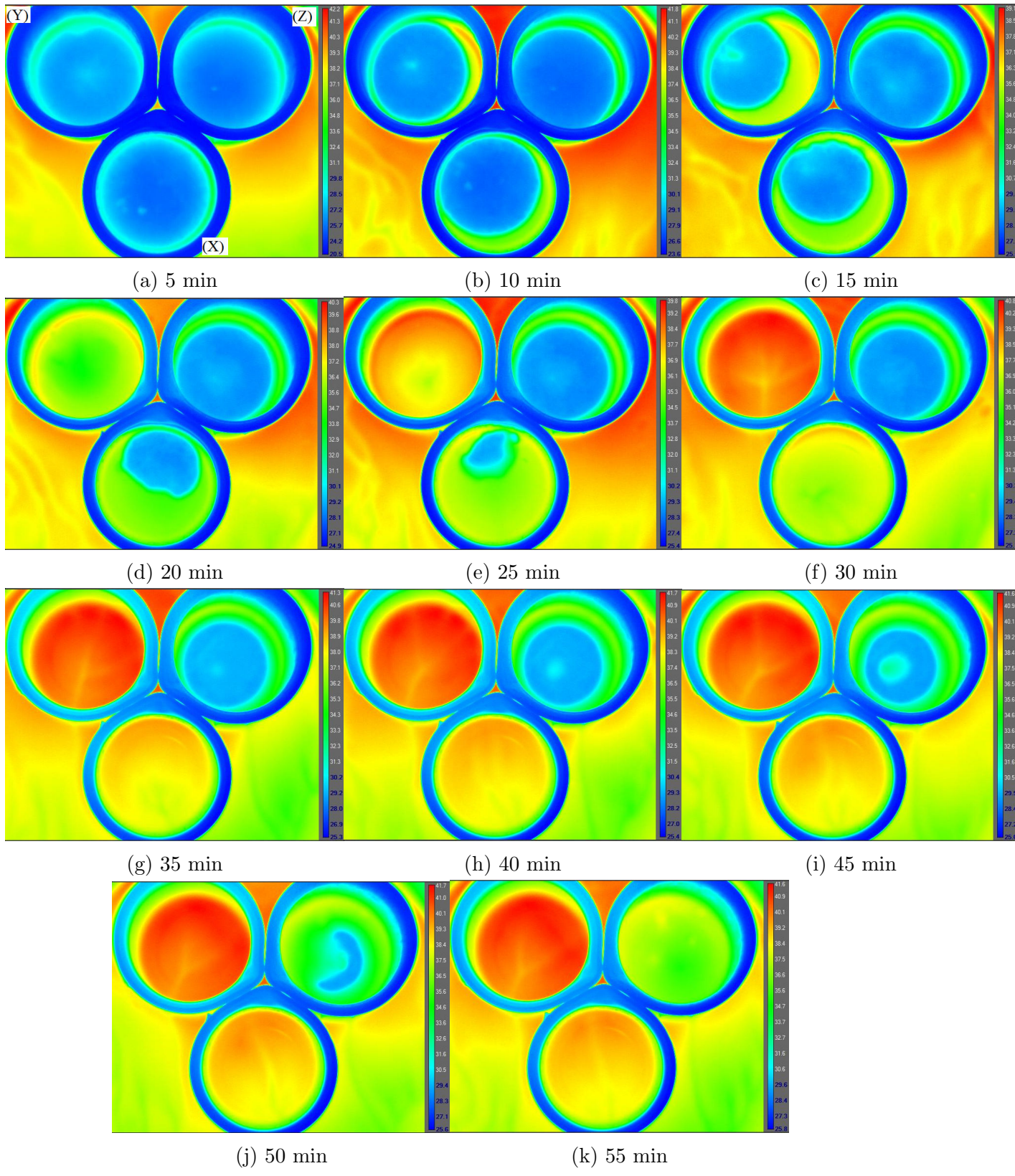
Figure 24: *Infrared thermography images of the melting process of RT–28HC-(X), RT–28HC/Al$_2$O$_3$+CuO-(Y) and RT–28HC/GNPs+MWCNTs-(Z) at different time steps with temperature variation in °C.*

## 4. Conclusions

An experimental study was conducted to investigate the thermal properties of carbon-based (GNPs and MWCNTs) and metallic oxide-based ($Al_2O_3$ and CuO) mono and hybrid NePCMs. The mass fraction of all the nanoparticles was kept constant of 1.0 wt.%, to explore the best NePCM with optimum thermal properties for efficient thermal management of microelectronics. Various material characteristic techniques such as ESEM, FT–IR, TGA, DCS, IRT and thermal conductivity apparatus were used to explore the chemical and thermal properties. The results of the current study are summarized as follows:

- The surface morphological and structural investigation disclosed the presence of GNPs, MWCNTs, $\gamma-Al_2O_3$ and CuO in pure RT–28HC. Furthermore, ESEM and XRD results confirmed the uniform dispersion of all the nanoparticles into RT–28HC.

- The FT–IR spectrum revealed the chemical compatibility of GNPs, MWCNTs, $\gamma-Al_2O_3$ and CuO with RT–28HC and only physical interaction of nanoparticles with RT–28HC was found.

- The TGA and DTG results revealed that all the mono and hybrid NePCMs maintained their thermal and chemical stability. The addition of nanoparticles improved the thermal and chemical stability of pure RT–28HC. Furthermore, the GNPs and MWCNTs dispersed NePCMs showed better dispersion stability than $Al_2O_3$ and CuO dispersed NePCM. In addition, hybrid NePCM of GNPs+MWCNTs nanoparticles had the better stability than $Al_2O_3$+CuO nanoparticles dispersed hybrid NePCM.

- Small variations were observed in the DSC results regarding melting temperature and latent heat of fusion. The maximum deviation in peak melting temperatures observed were $-0.17\%$ and $-0.14\%$ for RT–28HC/GNPs+MWCNTs and RT–28HC/$Al_2O_3$+CuO, respectively. Similarly, a maximum deviation of $-0.78\%$ and $-0.60\%$ were obtained in peak solidification temperatures for RT–28HC/GNPs+MWCNTs and RT–28HC/$Al_2O_3$+CuO, respectively. In addition, the maximum reduction in latent–heat of fusions were 3.75% and 2.44%, respectively, for RT–28HC/GNPs+MWCNTs and RT–28HC/$Al_2O_3$+CuO. Finally, the maximum reduction in latent–heat of solidification for RT–28HC/GNPs+MWCNTs and RT–28HC/$Al_2O_3$+CuO were 3.54% and 2.61%, respectively.

- The hybrid NePCM containing mass percentage ratio of 25%/75% GNPs+MWCNTs showed the higher thermal conductivity enhancement of 96% than GNPs and MWC-

NTs based NePCM having 71.4% and 61.2% thermal conductivity enhancement, respectively, compared to pure PCM. By comparison, a 49% enhancement in thermal conductivity of RT–28HC/Al$_2$O$_3$+CuO hybrid NePCM was achieved relative to pure PCM.

- The IRT results illustrated that RT–28HC/GNPs+MWCNTs hybrid NePCM showed uniform heating for a longer melting duration compared to RT–28HC/Al$_2$O$_3$+CuO and pure RT–28HC. This enhancement in phase transition of RT–28HC/GNPs+MWCNTs hybrid NePCM during heating was due to the uniform and homogenous dispersion of carbon-based nanoparticles (GNPs+MWCNTs) in organic PCMs, which increases the viscosity and shape–stability while lowering the convection heat transfer.

The results have proved that the prepared hybrid NePCMs exhibit significant enhancement in thermal properties without significantly affecting TES capability. Therefore, hybrid NePCMs may be used for passive thermal management of microelectronics after thermal cyclic tests.

**Conflict of interest**

The authors declare no conflict of interest regarding this research article.

**Acknowledgement**

# References

[1] A. Arshad, M. Jabbal, Y. Yan, J. Darkwa, The micro-/nano-pcms for thermal energy storage systems: A state of art review, International Journal of Energy Research 43 (11) (2019) 5572–5620. `arXiv:https://onlinelibrary.wiley.com/doi/pdf/10.1002/er.4550`, `doi:10.1002/er.4550`.
URL `https://onlinelibrary.wiley.com/doi/abs/10.1002/er.4550`

[2] D. Feng, Y. Feng, L. Qiu, P. Li, Y. Zang, H. Zou, Z. Yu, X. Zhang, Review on nanoporous composite phase change materials: Fabrication, characterization, enhancement and molecular simulation, Renewable and Sustainable Energy Reviews 109 (2019) 578–605. `doi:10.1016/j.rser.2019.04.041`.

[3] A. Arshad, H. M. Ali, M. Ali, S. Manzoor, Thermal performance of phase change material (PCM) based pin-finned heat sinks for electronics devices: Effect of pin thickness and PCM volume fraction, Applied Thermal Engineering 112 (2017) 143–155. `doi:10.1016/j.applthermaleng.2016.10.090`.

[4] M. J. Ashraf, H. M. Ali, H. Usman, A. Arshad, Experimental passive electronics cooling: Parametric investigation of pin-fin geometries and efficient phase change materials, International Journal of Heat and Mass Transfer 115 (2017) 251–263. `doi:10.1016/j.ijheatmasstransfer.2017.07.114`.

[5] H. M. Ali, A. Arshad, Experimental investigation of n-eicosane based circular pin-fin heat sinks for passive cooling of electronic devices, International Journal of Heat and Mass Transfer 112 (2017) 649–661. `doi:10.1016/j.ijheatmasstransfer.2017.05.004`.

[6] A. Arshad, H. M. Ali, W.-M. Yan, A. K. Hussein, M. Ahmadlouydarab, An experimental study of enhanced heat sinks for thermal management using n-eicosane as phase change material, Applied Thermal Engineering 132 (2018) 52–66. `doi:10.1016/j.applthermaleng.2017.12.066`.

[7] A. Arshad, H. M. Ali, S. Khushnood, M. Jabbal, Experimental investigation of PCM based round pin-fin heat sinks for thermal management of electronics: Effect of pin-fin diameter, International Journal of Heat and Mass Transfer 117 (2018) 861–872. `doi:10.1016/j.ijheatmasstransfer.2017.10.008`.

37

[8] H. M. Ali, A. Arshad, M. Jabbal, P. Verdin, Thermal management of electronics devices with PCMs filled pin-fin heat sinks: A comparison, International Journal of Heat and Mass Transfer 117 (2018) 1199–1204. `doi:10.1016/j.ijheatmasstransfer.2017.10.065`.

[9] H. M. Ali, A. Arshad, M. M. Janjua, W. Baig, U. Sajjad, Thermal performance of LHSU for electronics under steady and transient operations modes, International Journal of Heat and Mass Transfer 127 (2018) 1223–1232. `doi:10.1016/j.ijheatmasstransfer.2018.06.120`.

[10] M. Al-Jethelah, S. Ebadi, K. Venkateshwar, S. Tasnim, S. Mahmud, A. Dutta, Charging nanoparticle enhanced bio-based PCM in open cell metallic foams: An experimental investigation, Applied Thermal Engineering 148 (2019) 1029–1042. `doi:10.1016/j.applthermaleng.2018.11.121`.

[11] A. Allahbakhsh, M. Arjmand, Graphene-based phase change composites for energy harvesting and storage: State of the art and future prospects, Carbon 148 (2019) 441–480. `doi:10.1016/j.carbon.2019.04.009`.

[12] J. P. Tarelho, M. P. S. dos Santos, J. A. Ferreira, A. Ramos, S. Kopyl, S. O. Kim, S. Hong, A. Kholkin, Graphene-based materials and structures for energy harvesting with fluids – a review, Materials Today 21 (10) (2018) 1019–1041. `doi:10.1016/j.mattod.2018.06.004`.

[13] A. N. Keshteli, M. Sheikholeslami, Nanoparticle enhanced PCM applications for intensification of thermal performance in building: A review, Journal of Molecular Liquids 274 (2019) 516–533. `doi:10.1016/j.molliq.2018.10.151`.

[14] L. Fan, J. Khodadadi, Thermal conductivity enhancement of phase change materials for thermal energy storage: A review, Renewable and Sustainable Energy Reviews 15 (1) (2011) 24–46. `doi:10.1016/j.rser.2010.08.007`.

[15] Y. Lin, Y. Jia, G. Alva, G. Fang, Review on thermal conductivity enhancement, thermal properties and applications of phase change materials in thermal energy storage, Renewable and Sustainable Energy Reviews 82 (2018) 2730–2742. `doi:10.1016/j.rser.2017.10.002`.

[16] K. Y. Leong, M. R. A. Rahman, B. A. Gurunathan, Nano-enhanced phase change materials: A review of thermo-physical properties, applications and challenges, Journal of Energy Storage 21 (2019) 18–31. `doi:10.1016/j.est.2018.11.008`.

[17] S. Wu, T. Yan, Z. Kuai, W. Pan, Thermal conductivity enhancement on phase change materials for thermal energy storage: A review, Energy Storage Materials`doi:10.1016/j.ensm.2019.10.010`.

[18] D. H. Choi, J. Lee, H. Hong, Y. T. Kang, Thermal conductivity and heat transfer performance enhancement of phase change materials (PCM) containing carbon additives for heat storage application, International Journal of Refrigeration 42 (2014) 112–120. `doi:10.1016/j.ijrefrig.2014.02.004`.

[19] M. Li, M. Chen, Z. Wu, J. Liu, Carbon nanotube grafted with polyalcohol and its influence on the thermal conductivity of phase change material, Energy Conversion and Management 83 (2014) 325–329. `doi:10.1016/j.enconman.2014.04.002`.

[20] T. Li, J.-H. Lee, R. Wang, Y. T. Kang, Heat transfer characteristics of phase change nanocomposite materials for thermal energy storage application, International Journal of Heat and Mass Transfer 75 (2014) 1–11. `doi:10.1016/j.ijheatmasstransfer.2014.03.054`.

[21] L.-W. Fan, Z.-Q. Zhu, Y. Zeng, Y.-Q. Xiao, X.-L. Liu, Y.-Y. Wu, Q. Ding, Z.-T. Yu, K.-F. Cen, Transient performance of a PCM-based heat sink with high aspect-ratio carbon nanofillers, Applied Thermal Engineering 75 (2015) 532–540. `doi:10.1016/j.applthermaleng.2014.10.050`.

[22] D. Zou, X. Ma, X. Liu, P. Zheng, Y. Hu, Thermal performance enhancement of composite phase change materials (PCM) using graphene and carbon nanotubes as additives for the potential application in lithium-ion power battery, International Journal of Heat and Mass Transfer 120 (2018) 33–41. `doi:10.1016/j.ijheatmasstransfer.2017.12.024`.

[23] T. Nomura, C. Zhu, S. Nan, K. Tabuchi, S. Wang, T. Akiyama, High thermal conductivity phase change composite with a metal-stabilized carbon-fiber network, Applied Energy 179 (2016) 1–6. `doi:10.1016/j.apenergy.2016.04.070`.

[24] T. Nomura, K. Tabuchi, C. Zhu, N. Sheng, S. Wang, T. Akiyama, High thermal conductivity phase change composite with percolating carbon fiber network, Applied Energy 154 (2015) 678–685. `doi:10.1016/j.apenergy.2015.05.042`.

[25] F. Bahiraei, A. Fartaj, G.-A. Nazri, Experimental and numerical investigation on the performance of carbon-based nanoenhanced phase change materials for thermal management applications, Energy Conversion and Management 153 (2017) 115–128. `doi:10.1016/j.enconman.2017.09.065`.

[26] W. Yang, L. Zhang, Y. Guo, Z. Jiang, F. He, C. Xie, J. Fan, J. Wu, K. Zhang, Novel segregated-structure phase change materials composed of paraffin@graphene microencapsules with high latent heat and thermal conductivity, Journal of Materials Science 53 (4) (2017) 2566–2575. `doi:10.1007/s10853-017-1693-2`.

[27] Z. Ling, J. Chen, T. Xu, X. Fang, X. Gao, Z. Zhang, Thermal conductivity of an organic phase change material/expanded graphite composite across the phase change temperature range and a novel thermal conductivity model, Energy Conversion and Management 102 (2015) 202–208. `doi:10.1016/j.enconman.2014.11.040`.

[28] R. J. Warzoha, A. S. Fleischer, Effect of graphene layer thickness and mechanical compliance on interfacial heat flow and thermal conduction in solid–liquid phase change materials, ACS Applied Materials & Interfaces 6 (15) (2014) 12868–12876. `doi:10.1021/am502819q`.

[29] M. Bashar, K. Siddiqui, Experimental investigation of transient melting and heat transfer behavior of nanoparticle-enriched PCM in a rectangular enclosure, Journal of Energy Storage 18 (2018) 485–497. `doi:10.1016/j.est.2018.06.006`.

[30] X. Li, Y. Zhou, H. Nian, X. Zhang, O. Dong, X. Ren, J. Zeng, C. Hai, Y. Shen, Advanced nanocomposite phase change material based on calcium chloride hexahydrate with aluminum oxide nanoparticles for thermal energy storage, Energy & Fuels 31 (6) (2017) 6560–6567. `doi:10.1021/acs.energyfuels.7b00851`.

[31] M. Nourani, N. Hamdami, J. Keramat, A. Moheb, M. Shahedi, Thermal behavior of paraffin-nano-al2o3 stabilized by sodium stearoyl lactylate as a stable phase change material with high thermal conductivity, Renewable Energy 88 (2016) 474–482. `doi:10.1016/j.renene.2015.11.043`.

[32] M. Nourani, N. Hamdami, J. Keramat, A. Moheb, M. Shahedi, Preparation of a stable nanocomposite phase change material (NCPCM) using sodium stearoyl lactylate (SSL) as the surfactant and evaluation of its stability using image analysis, Renewable Energy 93 (2016) 404–411. doi:10.1016/j.renene.2016.02.073.

[33] L. Colla, L. Fedele, S. Mancin, L. Danza, O. Manca, Nano-PCMs for enhanced energy storage and passive cooling applications, Applied Thermal Engineering 110 (2017) 584–589. doi:10.1016/j.applthermaleng.2016.03.161.

[34] A. Babapoor, G. Karimi, S. Sabbaghi, Thermal characteristic of nanocomposite phase change materials during solidification process, Journal of Energy Storage 7 (2016) 74–81. doi:10.1016/j.est.2016.05.006.

[35] M. Chieruzzi, A. Miliozzi, T. Crescenzi, L. Torre, J. M. Kenny, A new phase change material based on potassium nitrate with silica and alumina nanoparticles for thermal energy storage, Nanoscale research letters 10 (1) (2015) 273.

[36] A. Babapoor, G. Karimi, Thermal properties measurement and heat storage analysis of paraffinnanoparticles composites phase change material: Comparison and optimization, Applied Thermal Engineering 90 (2015) 945–951. doi:10.1016/j.applthermaleng.2015.07.083.

[37] Y. Pahamli, M. Hosseini, A. Ranjbar, R. Bahrampoury, Effect of nanoparticle dispersion and inclination angle on melting of PCM in a shell and tube heat exchanger, Journal of the Taiwan Institute of Chemical Engineers 81 (2017) 316–334. doi:10.1016/j.jtice.2017.09.044.

[38] B. Praveen, S. Suresh, Experimental study on heat transfer performance of neopentyl glycol/CuO composite solid-solid PCM in TES based heat sink, Engineering Science and Technology, an International Journal 21 (5) (2018) 1086–1094. doi:10.1016/j.jestch.2018.07.010.

[39] R. Sharma, P. Ganesan, V. Tyagi, H. Metselaar, S. Sandaran, Thermal properties and heat storage analysis of palmitic acid-TiO 2 composite as nano-enhanced organic phase change material (NEOPCM), Applied Thermal Engineering 99 (2016) 1254–1262. doi:10.1016/j.applthermaleng.2016.01.130.

[40] L. Zhichao, Z. Qiang, W. Gaohui, Preparation and enhanced heat capacity of nano-titania doped erythritol as phase change material, International Journal of Heat and Mass Transfer 80 (2015) 653–659.

[41] N. Putra, S. Rawi, M. Amin, E. Kusrini, E. A. Kosasih, T. M. I. Mahlia, Preparation of beeswax/multi-walled carbon nanotubes as novel shape-stable nanocomposite phase-change material for thermal energy storage, Journal of Energy Storage 21 (2019) 32–39. `doi:10.1016/j.est.2018.11.007`.

[42] M. He, L. Yang, W. Lin, J. Chen, X. Mao, Z. Ma, Preparation, thermal characteri-zation and examination of phase change materials (PCMs) enhanced by carbon-based nanoparticles for solar thermal energy storage, Journal of Energy Storage 25 (2019) 100874. `doi:10.1016/j.est.2019.100874`.

[43] X. Zhang, C. Zhu, G. Fang, Preparation and thermal properties of n-eicosane/nano-SiO2/expanded graphite composite phase-change material for thermal energy storage, Materials Chemistry and Physics 240 (2020) 122178. `doi:10.1016/j.matchemphys.2019.122178`.

[44] 2-dtech ltd/versarien plc, nanene, accessed: 01/05/2019.
URL `https://www.2-dtech.com/products/`

[45] Industrial multi-walled carbon nanotubes (gcm597), carbon nanotubes plus, accessed: 01/05/2019.
URL `https://cnplus.us/inc/sdetail/403`

[46] Sodium dodecylbenzene sulfonate, sigma-aldrich, uk., accessed: 01/05/2019.
URL `https://www.sigmaaldrich.com/catalog/product/aldrich/289957?lang=en&region=GB`

[47] A. Asadi, I. M. Alarifi, V. Ali, H. M. Nguyen, An experimental investigation on the effects of ultrasonication time on stability and thermal conductivity of MWCNT-water nanofluid: Finding the optimum ultrasonication time, Ultrasonics Sonochemistry 58 (2019) 104639. `doi:10.1016/j.ultsonch.2019.104639`.

[48] D8 advance, bruker uk limited, accessed: 01/10/2019.
URL `https://www.bruker.com/products/x-ray-diffraction-and-elemental-analysis/x-ray-diffraction/d8-advance/overview.html`

[49] Ta instruments sdt-q600 simultaneous tga / dsc, artisan technology group, usa, accessed: 01/10/2019.

URL https://www.artisantg.com/Scientific/74393-1/TA_Instruments_SDT_Q600_Simultaneous_TGA_DSC

[50] Dsc 2500, ta instruments, uk, accessed: 01/10/2019.

URL https://www.tainstruments.com/dsc-2500/

[51] Tci thermal conductivity analyzer, c-therm technologies ltd. canada, accessed: 01/10/2019.

URL https://ctherm.com/products/tci_thermal_conductivity/

[52] M. Saterlie, H. Sahin, B. Kavlicoglu, Y. Liu, O. Graeve, Particle size effects in the thermal conductivity enhancement of copper-based nanofluids, Nanoscale Research Letters 6 (1) (2011) 217. doi:10.1186/1556-276x-6-217.

[53] W. Evans, R. Prasher, J. Fish, P. Meakin, P. Phelan, P. Keblinski, Effect of aggregation and interfacial thermal resistance on thermal conductivity of nanocomposites and colloidal nanofluids, International Journal of Heat and Mass Transfer 51 (5-6) (2008) 1431–1438.

[54] F. Bakhtiari, E. Darezereshki, One-step synthesis of tenorite (CuO) nano-particles from cu4 (SO4) (OH) 6 by direct thermal-decomposition method, Materials Letters 65 (2) (2011) 171–174. doi:10.1016/j.matlet.2010.09.071.

[55] M. Faisal, S. B. Khan, M. M. Rahman, A. Jamal, A. Umar, Ethanol chemi-sensor: Evaluation of structural, optical and sensing properties of CuO nanosheets, Materials Letters 65 (9) (2011) 1400–1403. doi:10.1016/j.matlet.2011.02.013.

[56] E. Lestari, I. Saptiama, H. Setiawan, et al., Synthesis of nano-$\alpha$-al 2 o 3 for 99 mo adsorbent, Atom Indonesia 44 (1) (2018) 17–21.

[57] D. Mei, B. Zhang, R. Liu, Y. Zhang, J. Liu, Preparation of capric acid/halloysite nanotube composite as form-stable phase change material for thermal energy storage, Solar Energy Materials and Solar Cells 95 (10) (2011) 2772–2777. doi:10.1016/j.solmat.2011.05.024.

[58] M. Mehrali, S. T. Latibari, M. Mehrali, H. S. C. Metselaar, M. Silakhori, Shape-stabilized phase change materials with high thermal conductivity based on paraffin/graphene oxide composite, Energy conversion and management 67 (2013) 275–282.

[59] T. M. Keller, S. B. Qadri, C. A. Little, Carbon nanotube formation in situ during carbonization in shaped bulk solid cobalt nanoparticle compositions, Journal of Materials Chemistry 14 (20) (2004) 3063. `doi:10.1039/b402936d`.

[60] S. Åsbrink, L. J. Norrby, A refinement of the crystal structure of copper(II) oxide with a discussion of some exceptional e.s.d.s, Acta Crystallographica Section B Structural Crystallography and Crystal Chemistry 26 (1) (1970) 8–15. `doi:10.1107/s0567740870001838`.

[61] X. xiang Zhang, Y. feng Fan, X. ming Tao, K. lun Yick, Crystallization and prevention of supercooling of microencapsulated n-alkanes, Journal of Colloid and Interface Science 281 (2) (2005) 299–306. `doi:10.1016/j.jcis.2004.08.046`.

[62] S. Yu, X. Wang, D. Wu, Self-assembly synthesis of microencapsulated n-eicosane phase-change materials with crystalline-phase-controllable calcium carbonate shell, Energy & Fuels 28 (5) (2014) 3519–3529. `doi:10.1021/ef5005539`.

[63] M. Anwar, F. Turci, T. Schilling, Crystallization mechanism in melts of short n-alkane chains, The Journal of Chemical Physics 139 (21) (2013) 214904. `doi:10.1063/1.4835015`.

[64] M. Oliver, P. Calvert, Homogeneous nucleation of n-alkanes measured by differential scanning calorimetry, Journal of Crystal Growth 30 (3) (1975) 343–351. `doi:10.1016/0022-0248(75)90010-x`.

[65] A. M. Taggart, F. Voogt, G. Clydesdale, K. J. Roberts, An examination of the nucleation kinetics ofn-alkanes in the homologous series c13h28to c32h66, and their relationship to structural type, associated with crystallization from stagnant melts, Langmuir 12 (23) (1996) 5722–5728. `doi:10.1021/la9600816`.

[66] H. Kraack, E. B. Sirota, M. Deutsch, Measurements of homogeneous nucleation in normal-alkanes, The Journal of Chemical Physics 112 (15) (2000) 6873–6885. `doi:10.1063/1.481263`.

[67] F. Yavari, H. R. Fard, K. Pashayi, M. A. Rafiee, A. Zamiri, Z. Yu, R. Ozisik, T. Borca-Tasciuc, N. Koratkar, Enhanced thermal conductivity in a nanostructured phase change composite due to low concentration graphene additives, The Journal of Physical Chemistry C 115 (17) (2011) 8753–8758. `doi:10.1021/jp200838s`.

[68] H. Tian, W. Wang, J. Ding, X. Wei, M. Song, J. Yang, Thermal conductivities and characteristics of ternary eutectic chloride/expanded graphite thermal energy storage composites, Applied Energy 148 (2015) 87–92. `doi:10.1016/j.apenergy.2015.03.020`.

[69] J. Wang, H. Xie, Z. Xin, Thermal properties of paraffin based composites containing multi-walled carbon nanotubes, Thermochimica Acta 488 (1-2) (2009) 39–42. `doi:10.1016/j.tca.2009.01.022`.

[70] O. Mahian, L. Kolsi, M. Amani, P. Estellé, G. Ahmadi, C. Kleinstreuer, J. S. Marshall, M. Siavashi, R. A. Taylor, H. Niazmand, S. Wongwises, T. Hayat, A. Kolanjiyil, A. Kasaeian, I. Pop, Recent advances in modeling and simulation of nanofluid flows-part i: Fundamentals and theory, Physics Reports 790 (2019) 1–48. `doi:10.1016/j.physrep.2018.11.004`.